New insights on the fault structure of a geothermal testbed and the associated seismicity based on active seismic tomography

Miriam Larissa Schwarz[1], Hansruedi Maurer[2], Anne Obermann[1,2], Paul Antony Selvadurai[1],
Alexis Shakas[2], Stefan Wiemer[1], and Domenico Giardini[2]

[1]Swiss Seismological Service, ETH Zürich, Sonneggstrasse 5, CH-8092 Zürich
[2]Institute of Geophysics, ETH Zürich, Sonneggstrasse 5, CH-8092 Zürich

Correspondence: Miriam Larissa Schwarz (miriam.schwarz@sed.ethz.ch)

Abstract. ~~For obtaining~~ To obtain reliable high-resolution subsurface images in the geothermal testbed of the Bedretto Underground Laboratory for Geosciences and Geoenergies (BedrettoLab), we ~~have~~ applied fat ray travel time tomography ~~.~~ ~~To compute~~ with the aim of better understanding the relationship between structural features and the seismicity induced by hydraulic stimulation tests. For the computation a 3D velocity model, we ~~made use of 8~~ utilized eight boreholes, which ~~allowed us to compile~~ provided us with a large data set ~~including~~ comprising 42’843 manually picked first breaks. ~~We~~ Our results demonstrate that the fat ray approach offers improved image quality compared ~~with~~ to traditional ray-based methods. ~~Furthermore, we have validated the~~ The 3D model was further validated using ground-truth information from wireline logs and geological observations. We ~~succeeded in imaging~~ successfully imaged a major fault zone (MFZ) that ~~has a rather~~ exhibits a complex structure including considerable heterogeneity. Relocation of passive seismic events ~~,~~ generated during hydraulic stimulations ~~, indicate~~ indicates that the 3D velocity model has only a minor influence on ~~the hypocentral parameters, but a comparison of~~ hypocentral parameters. However, comparing a selection of ~~particularly~~ well-constrained seismic events with the velocity structures revealed ~~that there is~~ a remarkable spatial correlation. Most events occurred in regions of intermediate and slightly decreased seismic velocities, thereby ~~"avoiding " high and very low velocity areas~~avoiding both high- and very low-velocity zones. Based on small-scale laboratory studies, we speculate that these observations can be ~~attributed to the occurrence~~ explained by the presence of stress gradients in the ~~intermediate velocity~~ intermediate-velocity zones.

Copyright statement.

1 Introduction

Energy production from sustainable resources is a key challenge of this century. ~~In this context, geothermal~~ Geothermal energy is recognized as a viable option. In particular, so-called “enhanced geothermal systems” (EGS) may have the potential to produce electrical energy at affordable costs (e.g. Olasolo et al. (2016); Hirschberg et al. (2015)). Key challenges include establishing sustainable flow rates, while controlling the associated induced seismicity Zang et al. (2024). Examples of EGS projects that had to be stopped ~~because of~~ due to high seismicity include, for example, Basel (Edwards et al., 2015) and Pohang (Ellsworth et al., 2019). These problems are closely linked with the often poorly known fracture network of the reservoir. Therefore, several initiatives have been established to better characterize relevant host rock structures with near-field observations and well-monitored stimulation experiments. (Amann et al., 2018; Obermann et al., 2024; Kneafsey et al., 2025).

~~In this context, seismic measurements~~ Seismic studies can offer powerful tools for imaging key structures, such as permeable fracture zones~~that~~ , which are the main targets of EGS investigations. They can be applied during an initial ~~characterisation~~ characterization phase or during the stimulation phase. Generally, it can be distinguished ~~between~~ by passive and active seismic techniques. Passive techniques do not require actively fired seismic sources. Instead, either information contained in the ambient noise is exploited (e.g., Obermann and Hillers (2019)) or recordings from the induced seismicity are analyzed. For example, Charléty et al. (2006) conducted a 4D tomographic study using induced seismicity at the Soultz-sous-Forêts Hot Dry Rock site in France~~.~~ , that is, temporal 3D seismic velocity ~~structures were obtained at different times to image the temporal changes in a 4D manner~~changes were computed.

Active seismic methods can generally be subdivided in reflection and refraction imaging and transmission tomography. Reflection and refraction imaging can be carried out either from the surface, or surface-to-borehole configurations - also referred as vertical seismic profiling (VSP) techniques. In geothermal applications, VSP is particularly popular. For example, Nakata et al. (2023) used VSP data for reflection imaging of faults and fractures at the geothermal test site FORGE, Utah, U.S.A.. It is also possible to combine induced seismicity methods with reflection imaging. Block et al. (1994) applied a joint hypocenter-velocity inversion using induced seismicity from Hot dry rock (HDR) experiments at Los Alamos National Laboratory, New Mexico to gain a 3D velocity model. Nakagome et al. (1998) used a seismic reflection survey together with vertical seismic profiling (VSP) to image the fractured reservoir in the Kakkonda geothermal field (Japan). Place et al. (2011) employed induced seismicity and VSP data to map fractures in Soultz-Sous-Fôrets (France). Transmission tomography primarily makes use of direct, diving or refracted waves traveling from sources to the receivers. It can be either applied from the surface (e.g., Zelt and Barton (1998); Lanz et al. (1998); Heincke et al. (2006)), or between boreholes (e.g., Pratt and Worthington (1988); Maurer and Green (1997)). Here, the travel times of the first arriving waves are exploited to establish 2D or 3D distributions of the seismic velocities. Alternatively, the first break amplitudes can be used to compute attenuation models (e.g., Holliger et al. (2001)). All these studies provided useful information for a better understanding of the subsurface structures.

Since seismic waves travel in a heterogeneous medium along complicated wave paths, 2D tomographic investigations suffer from inherent limitations, resulting from the assumption that the wave paths lie exclusively within the tomographic (2D) plane. Therefore, 3D investigations should be carried out, when complex subsurface structures are expected. This can be achieved quite easily with surface-based investigations, because the sources and receivers can be well distributed over the earth's surface, which results in a good seismic ray coverage of the structures of interest, given that acquisition offset is large enough. In the case of crosshole investigations, this is often a problem, because there are rarely enough boreholes available that allow a good ray coverage of the subsurface region of interest. Therefore, 3D crosshole tomography experiments are very rare, which is unfortunate, because they can potentially offer very relevant and unique subsurface information. The problem of poor ray coverage can be, at least partially, alleviated with the concept of fat rays~~. Here,~~ , where it is assumed that seismic waves are not traveling along infinitesimally thin rays, but within "fat rays", whose thickness is governed by the dominant frequencies of the seismic waves (e.g. Woodward, 1992). Initial concepts were provided by Woodward (1992), and fat ray approaches were implemented for local earthquake tomography (Husen and Kissling, 2001) and active seismic experiments (Jordi et al., 2016). ~~In~~ We have applied these concepts in the framework of the host rock characterization ~~of~~ in the Bedretto Lab (Ma et al., 2022; Plenkers et al., 2022)~~, an unusually large number of~~. As discussed in more detail in Section 2, this is a unique research environment including a geothermal testbed, which mimics a realistic reservoir structure in crystalline rocks. For example, it includes important structures, such as a major fault zone (MFZ). In total, nine boreholes were drilled within ~~a geothermal testbedat hectometer scale. Such a setup is particularly useful for~~ the geothermal testbed, out of which eight were available for active seismic measurements. This offered exciting opportunities for testing the benefits and limitations of 3D travel time tomography~~, making it possible to illuminate the entire volume of interest. Consequently, various~~. As described in this contribution, several active seismic crosshole measurements were carried out~~. In addition to the good borehole coverage, we benefited from the advantageous features of~~, and they were analyzed with a fat ray tomography ~~, and we could establish a well-constrained 3D velocity model that is valuable for characterizing critical host rock structures~~approach. The primary aim of our study is to image important geological structures, and to better understand the relationship between these structural features and the seismicity, induced by various hydraulic stimulation experiments within the geothermal testbed.

We start with a ~~short~~ description of the Bedretto Lab~~and~~, the embedded geothermal testbed, and we briefly summarize key results from previous investigations in the BedrettoLab. Then, we present our data set, followed by a short description of the methodology employed to establish the 3D velocity models. After the presentation of the tomographic results, we perform a joint interpretation with geological and geophysical add-on data sets that were also acquired at our test site. In particular, we discuss the spatial correlation between passive seismic events and the velocity structures found.

2 Site description

The Bedretto Underground Laboratory for Geosciences and Geoenergies (BULGG or BedrettoLab), operated by ETH Zurich, is located in the central Swiss Alps (Ticino) in a 5.2 kilometres long side tunnel of the Furka railway tunnel (Figure 1a). The BedrettoLab is a unique research facility that provides optimal conditions for conducting experimental research on understanding the responses of the deep underground during hydraulic stimulations. With dimensions at the hectometer scale (hundreds of meters extension), the BedrettoLab closes the gap between the decameter laboratory scale (tens of meters extension, e.g., Grimsel test site (Gischig et al., 2020)) and the reservoir scale ~~(Amann et al., 2018)~~(hundreds of meters to kilometers, (Amann et al., 2018)).

The BedrettoLab host rock is ~~called~~ composed of mainly granites, which are referred to as the Rotondo Granite. Its intrusion into the Gotthard Massif took place during the late Variscan orogeny (Sergeev et al. (1995)). In general, the Rotondo Granite is ~~relatively homogeneouswith only slight influences of metamorphism (Labhart T, 2005; Lützenkirchen and Loew, 2011) . The general maximum horizontal stress direction lies within the NW quadrant (Heidbach et al., 2018). Bröker and Ma (2022) discussed the effect of variations in the topography along the tunnel that can cause fluctuations of the local stress field . A previous study of Meier (2017) revealed that the topographic effect decreases with increasing overburdenand can be neglected~~

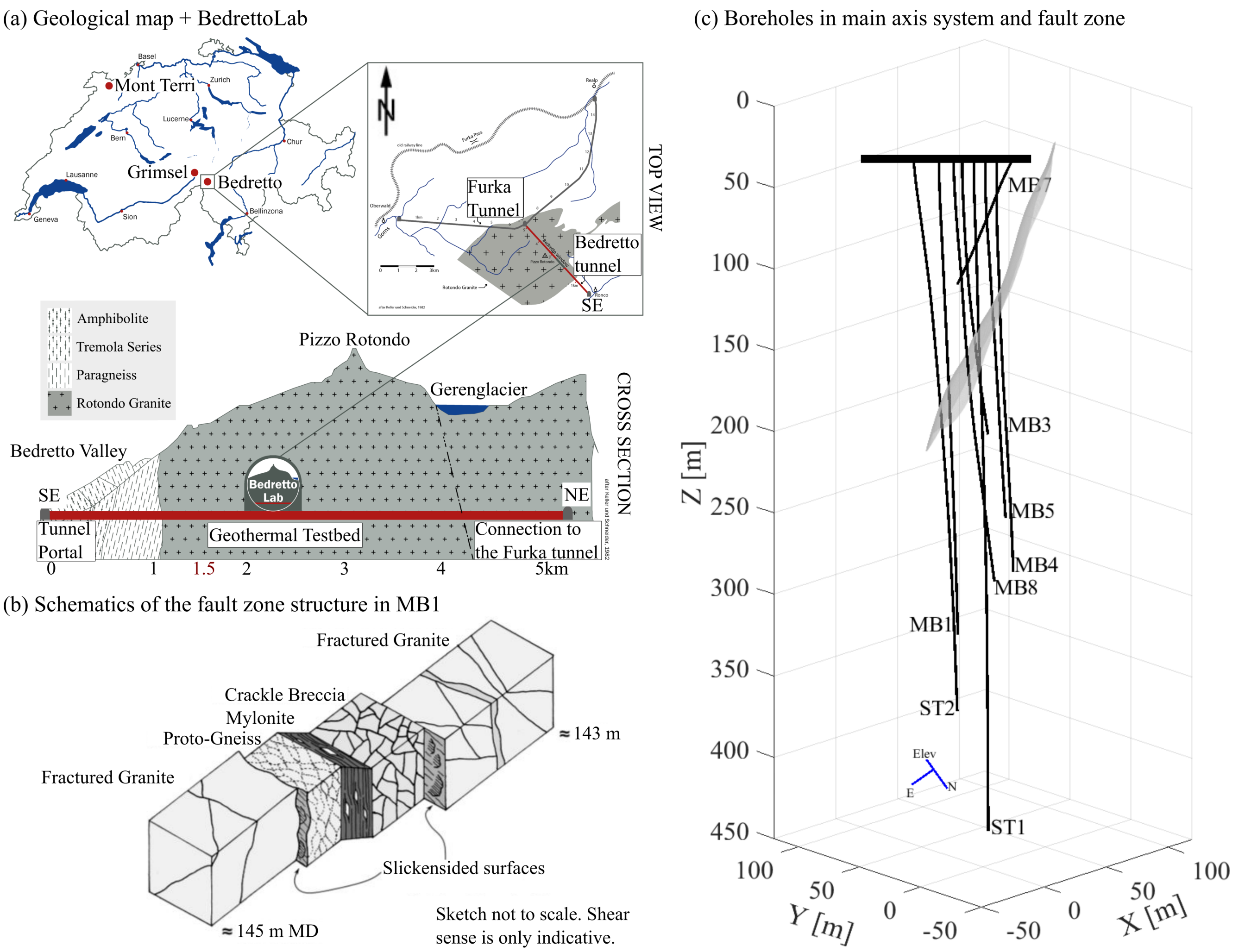

(a) Geological map + BedrettoLab

(c) Boreholes in main axis system and fault zone

(b) Schematics of the fault zone structure in MB1

Figure 1. (a) Location and geological map of the BedrettoLab (see also Ceccato et al. (2024) and Rast et al. (2022)). (b) Schematics of the ~~fault zone measured from~~ Major Fault Zone (MFZ), as observed in borehole MB1. The ~~fault zone~~ MFZ is found between 143 and 145 m depth in this borehole. Fractured Granites surround Porto-Gneis, Myolonite and Crackle Beccia ~~. Figure~~ (figure adjusted from Ma et al. (2022)). (c) ~~The~~ Boreholes drilled into the Geothermal Testbed~~contains~~ , including six monitoring boreholes (MB1, MB3-MB5, MB7, MB8)~~and~~ , one stimulation (ST1) and one extraction (ST2) borehole~~with lengths between 100 and 400 m~~. ~~The~~ Here, the boreholes are ~~rotated into~~ shown in the tomography coordinate system~~. The advantages of the rotation are a smaller amount of model parameters and positive axes for the inversion~~, which was used in this paper. The blue arrows show the orientation of the original Bedretto coordinate system with Easting, Northing and Elevation, ~~which is~~ as used in ~~many other BedrettoLab-related publications~~panel a). ~~The main fault zone in this area is shown as~~ Additionally, panel c) depicts the 3D structure of the MFZ (gray surface~~and is referred to as "Major Fault Zone" (MFZ)~~) ~~within this paper (fault zone after~~ as derived by Escallon et al. (2024)~~). For the following analysis this representation is used~~.

~~after tunnel meter 1500 m, where it is~~ homogeneous, that is, it generally exhibits isotropic structures, but at some places, weak signs of metamorphism are observed, (Labhart T, 2005; Lützenkirchen and Loew, 2011). This may have slightly altered the isotropic structures (see also Figure 1b). Indeed, Behnen et al. (2024) identified weak signs of anisotropy near the geothermal testbed, but for the sake of simplicity, we assume an isotropic velocity structure for this study.

According to the World Stress Map (Heidbach et al., 2018), the main horizontal compressive stresses are oriented in NW-SE direction, but Bröker et al. (2024a) showed that within the BedrettoLab, the orientation of the stress field can exhibit significant variations. Due to the overburden, the principal stress axis can be assumed to be vertical~~. There are some indications of a slight anisotropy of the host rock, which is expected to also affect the seismic velocities (Behnen et al., 2024), but for the sake of simplicity, we assume an isotropic velocity model~~, and a previous study of Meier (2017) revealed that topographic effects can be neglected in the area of the BedrettoLab.

The geothermal testbed is located between tunnel meters 2000 m to 2100 m, measured from the tunnel portal (see Figure 1a)). It has an overburden of about 1030 m~~. It~~ , and includes several boreholes, ranging from 250 m to 400 m length. The six monitoring boreholes (MB1, MB3-MB5, MB7, MB8) are equipped with a state-of-the-art monitoring system. This includes seismic sensors (geophones, accelerometers and acoustic emission sensors) as well as active ~~seismic sources (piezoelectric transducers)~~piezoelectric seismic sources. In addition, a stimulation (ST1) and an extraction (ST2) borehole were drilled into the testbed. ST1 was equipped with a multi-packer system, with which it was subdivided into 14 intervals ~~(?), and~~ (Bröker et al., 2024a). ST2 was kept open for the use of various measurements, for example, active seismic measurements~~with the P-wave sparker~~. For more details on the multi-disciplinary monitoring system, we refer to the overview paper of Plenkers et al. (2022).

Faults and fractures within the geothermal testbed have been mapped mainly as subvertically dipping, predominantly striking NE-SW to ENE-WSW (Labhart T, 2005; Lützenkirchen and Loew, 2011) and frequently steeply dipping, striking N-S and E-W along the tunnel (Jordan, 2019). Ma et al. (2022) and ~~?~~ Bröker et al. (2024b) show detailed maps of fractures along the tunnel, which are based on tunnel wall mapping and borehole logging. The fractures can be divided into four different sets: striking N–S, NE-SW/tunnel perpendicular, E–W, and NW–SE/tunnel parallel.

A major fault zone (MFZ) within the geothermal testbed is of particular interest for this ~~study~~paper. It was discovered by previous studies using all ~~boreholes available . Escallon et al. (2024) imaged the MFZ using GPR reflection measurements, and this was validated by borehole televiewer observations~~ available boreholes. This included core analyses as well as acoustic and optic televiewer (ATV/OTV) ~~that have been described by Ma et al. (2022). The MFZis shown as a gray surface~~ observations (Ma et al., 2022). A schematic of the MFZ, as observed in borehole MB1, is shown in Figure 1~~c). Ma et al. (2022) gives a schematic of the fault zone structure based on borehole cores (Figure 1d): the fault zone in MB1 ranges from 143 m-145 m MD (measured depth). Fractured Granite surrounds Proto-Gneis, Mylonite and Crackle Breccia~~b. It includes Proto-Gneis, Mylonite and Crackle Breccia that surround fractured granites. More details on this structures can be found in Ma et al. (2022), but for the purpose of this paper is primarily important to note that the complexity of the MFZ will represent a challenge for the tomographic imaging. Besides the a priori information, offered by the core and televiewer analyses, we also have access to a 3D image of the MFZ. It was obtained with a borehole radar reflection study (Escallon et al., 2024) , and the 3D surface of the

MFZ is shown in gray in Figure 1c.

Since we will later relate our tomographic inversions with the seismicity, generated by hydraulic stimulations, it is important to note that the BedrettoLab lies in an area of generally low seismicity (e.g. Diehl et al. (2025), Gischig et al. (2020)). All the seismic events, discussed later in this study, are caused by stimulations within the geothermal testbed, and they are not superimposed by a seismic background activity. Furthermore, it is also important to note that the stress conditions in the BedrettoLab mimic stress conditions of a real geothermal reservoir, but the temperatures are much lower (approx. 18 degrees Celsius, Ma et al. (2022)).

3 Data

~~Within the scope of~~ Although the geological and geophysical studies discussed in Section 2 provided key information for the characterization of the ~~geothermal testbed, a large variety of geophysical and geological measurements were carried out. This included~~ Geothermal Testbed, it was judged to be necessary to obtain additional volumetric information. This can be obtained from active seismic crosshole measurements. The full ~~data set contains~~ active seismic data set, employed in this study, is composed of several independent surveys that were taken at different times from October 2020 to November 2021, depending on when the boreholes were drilled and being available. A detailed overview is given in Table 1. The borehole configuration is shown in Figures 1b and 1c. The spacing of the source varied between 1 m, 2 m, and 5 m for the different surveys and along the borehole depths.

~~As a source we~~

We employed a seismic P-wave sparker source with a dominant frequency band of about 1 to 10 kHz (https://geotomographie.de). The first three data sets were recorded on two hydrophone chains with 1 m and 2 m spacing, respectively (Table 1). The surveys were designed, such that the receiver/shot spacing is denser around the MFZ and sparser at larger distances away from it. These surveys were conducted before the instrumentation and cementation of the boreholes. The last survey was carried out in November 2021, after the instrumentation, but prior to stimulation experiments. Permanently installed acoustic emission (AE) sensors were used as receivers, ~~and they~~ which had to be synchronized with the sparker setup. For each source point and all surveys, the sparker source was fired three times, and the traces were then stacked to enhance the signal-to-noise (SNR) ratio. Overall, we were able to compile a relatively large data set including 42’843 manual P-picks (Table 1) with ~~a~~ an average picking uncertainty of about 0.15 ms. This value was estimated on the basis of visual inspections during the manual picking process. Source-receiver ~~distances~~ offsets varied between 10 m and 186.5 m. For the manual picking, we employed a Matlab-based in-house software.

In Figure 2, we show three examples of shot and receiver gathers. Figure 2a) shows the setting with the source and receiver configurations as well as the MFZ. 2b) displays a receiver gather recorded on the AE sensors (sensor in MB8, sources in ST2), 2c) shows a receiver gather recorded on a hydrophone (sensor in MB5 and receiver in MB8) and 2d) shows a source gather recorded on hydrophones (source position in MB5 and receivers in MB8). The first arrivals of the P-waves, indicated by the yellow arrows, are clearly visible. The P-wave sparker, as the name suggests, is designed to generate primarily seismic P-waves.

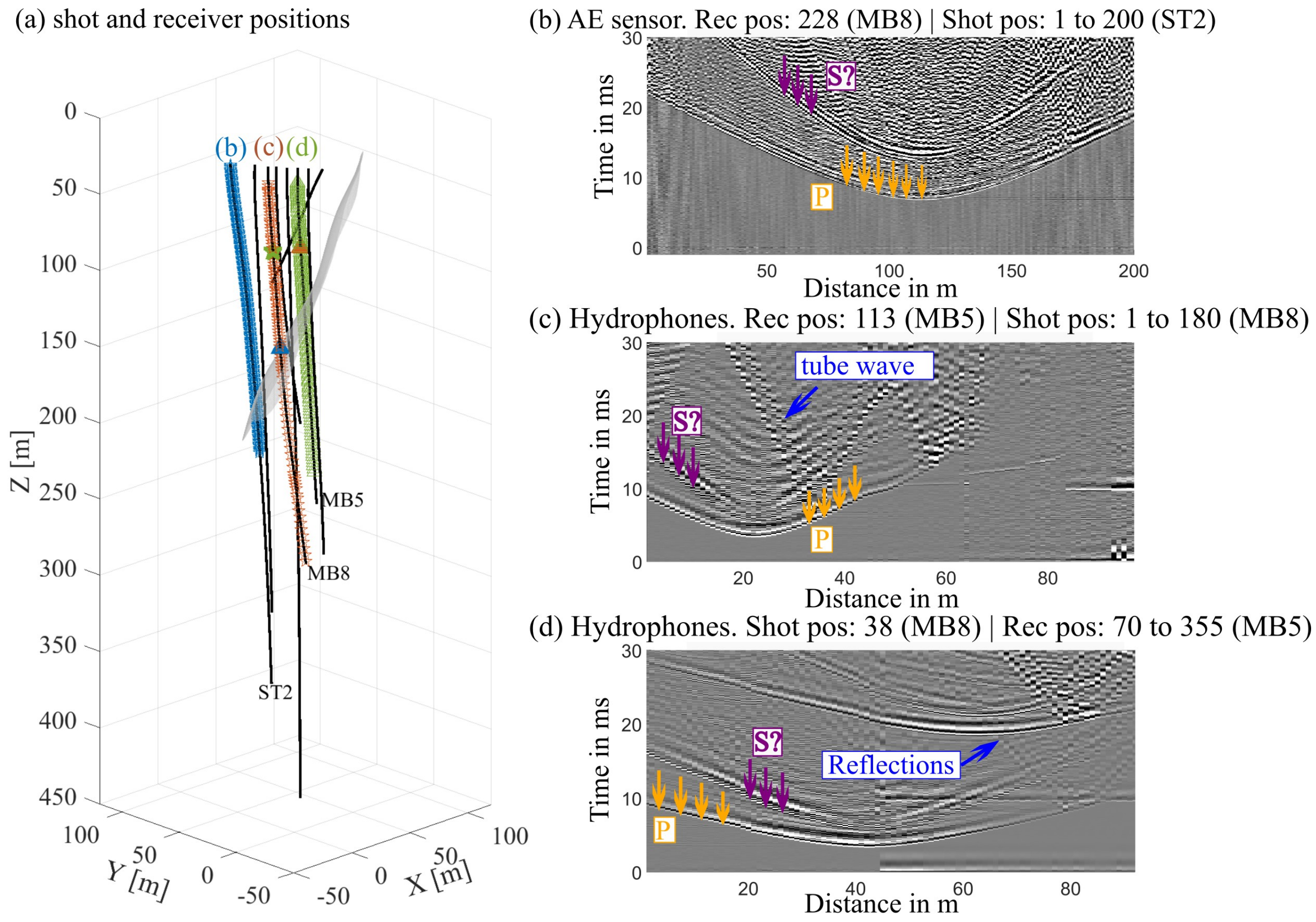

(a) shot and receiver positions

(b) AE sensor. Rec pos: 228 (MB8) | Shot pos: 1 to 200 (ST2)

(c) Hydrophones. Rec pos: 113 (MB5) | Shot pos: 1 to 180 (MB8)

(d) Hydrophones. Shot pos: 38 (MB8) | Rec pos: 70 to 355 (MB5)

Figure 2. ~~Shot~~ Experimental setup and ~~receiver gather~~data examples. ~~Figure~~ a) shows the shot (stars) and receiver (triangles) positions for the waveforms shown in b), c) and d). The ~~grey~~ gray surface indicates the MFZ as derived by Escallon et al. (2024). b) displays the ~~receiver gather~~ waveforms recorded ~~on the~~ by an AE sensors ~~,~~ in borehole MB8 (blue triangle) from shots in borehole ST2 (blue stars). c) shows a corresponding receiver gather recorded on a hydrophone in MB5 (brown triangle) and shots in borehole MB8 (brown stars). d) shows a ~~source~~ shot gather ~~recorded on~~ from a ~~hydrophone~~source in MB8 (green star) with hydrophones in MB5 (green triangles). First arrivals for P-wave are indicated with yellow arrows, and examples for reflections and tube wave are indicated with blue arrows. ~~Red arrows denote systematic noise patterns of unknown origin.~~ The predicted S-wave arrivals are indicated with purple arrows.

Table 1. Acquisition parameters of the active seismic survey

borehole source	borehole receiver	shot spacing	receiver spacing	sensor	da
ST1	ST2	2 m	1m/2m	hydrophones	Oct.
MB4	MB1	2 m	1 m	hydrophones	Oct.
MB3	MB4	2 m	1 m	hydrophones	Oct.
MB3	MB1	2 m	1 m	hydrophones	Oct.
MB1	MB4	2 m	1 m	hydrophones	Oct.
MB8	MB7	5 m/2 m	1 m/2 m	hydrophones	June
MB8	MB5	5 m/2 m	1 m/2 m	hydrophones	June
MB5	MB7	5 m/2 m	1 m/2 m	hydrophones	June
MB5	MB8	5 m/2 m	1 m/2 m	hydrophones	June
ST2	MB1	1 m	fixed depth	AE sensors	Nov.
ST2	MB3	1 m	fixed depth	AE sensors	Nov.
ST2	MB4	1 m	fixed depth	AE sensors	Nov.
ST2	~~MB4 1 m fixed depth AE sensors Nov. 2021 1200 667 ST2~~ MB5	1 m	fixed depth	AE sensors	Nov.
ST2	MB7	1 m	fixed depth	AE sensors	Nov.
ST2	MB8	1 m	fixed depth	AE sensors	Nov.
total number of source points:	649				
total number of receiver points:	962				
total number of traces:	74875				
total number of picks:	42843 (57.2 %)				
source type:	P-wave sparker				
sampling frequency					
hydrophones:	48 kHz				
AE sensors:	200 kHz				

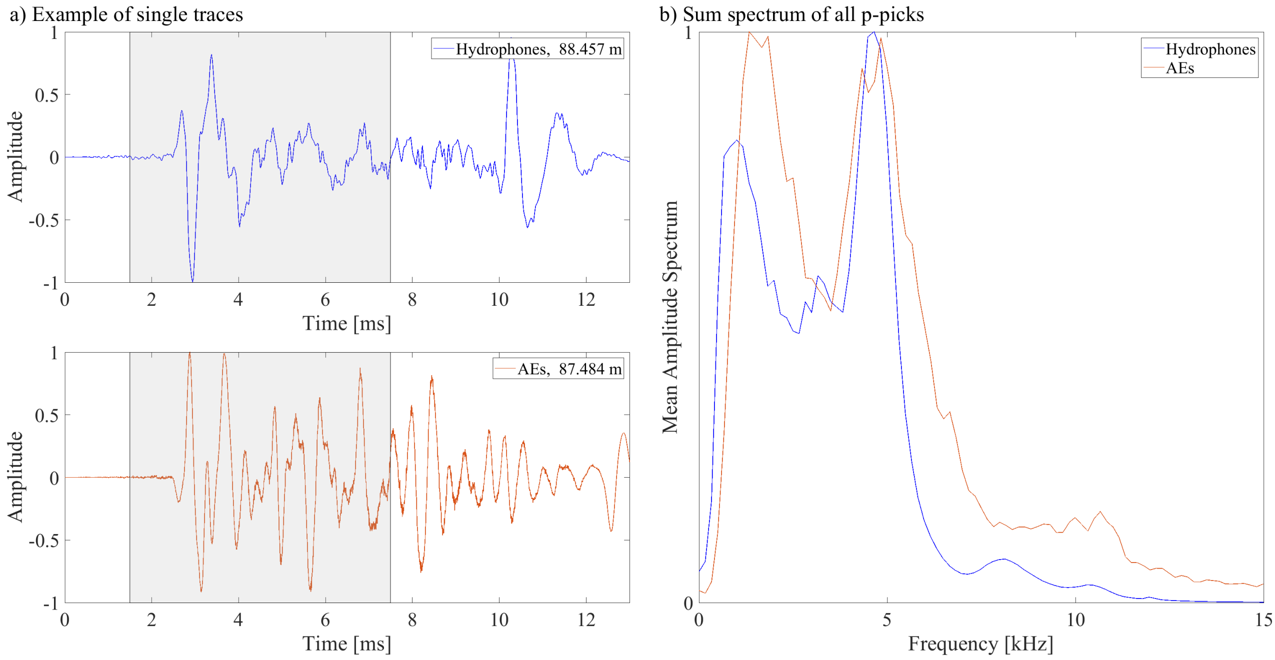

Figure 3. a) Example traces of ~~the data. Top: single trace of the~~ a hydrophone ~~data. Bottom: single trace recorded on~~ (top) and an ~~Acoustic Emission~~ AE sensor (~~AE~~bottom) ~~, both show a nice signal-to-noise ratio. Both signals are~~ that were recorded at ~~a~~ similar source-receiver ~~distance~~offsets. The ~~grey box~~ gray boxes indicates the time window that ~~is~~ was used to calculate the sum spectra shown in b) . For visualisation purposes, we normalized the data to the maximum amplitude. b) shows the sum ~~spectrum~~ spectra of all ~~p-picks, which reveals~~ traces with a ~~frequency band between 1 kHz and 7.5 kHz. We normalized~~ P pick (see main text for further explanations on the computation of the sum ~~spectrum for a better comparison~~spectra).

S-waves that are visible in the data are therefore most likely converted P-to-S phases, with the conversion likely taking place at the source borehole wall. The S-waves are ~~shown~~ marked in Figures 2b, c, and d, (indicated with purple arrows). They are generally difficult to pick, because they often overlap with scattered parts of the P-waves or with reflected waves. Therefore, we restrict ourselves to the first arriving P waves.

Figure 3a shows example traces from a hydrophone and an AE sensor with a similar source-receiver ~~distance. Furthermore, the summed amplitude spectrum of the P-wave for all~~ offset. Both traces show a high signal-to-noise ratio. To further appraise the properties of the seismic waveforms, we computed sum spectra for the hydrophone and AE sensor ~~recordings, where a first break onset could be picked, is shown~~data. For that purpose, all traces with a P pick were considered. A time window of 6 ms around the first break was ~~taken~~ considered to calculate the amplitude spectra ~~, which~~ (gray boxes in Figure 3a). The amplitude spectra of the individual traces were then summed up to obtain the sum ~~spectrum.~~spectra.

The frequency content of both sensor types is comparable, with the energy of the first-arriving waves varying between 1 kHz and 7.5 kHz. It should be noted that the sharp decrease below 1 kHz is caused by analog filters of the acquisition systems.

Furthermore, it is noteworthy that there is a significant decrease of spectral amplitudes around 3 kHz for both sensor types. ~~Since~~ One may argue that this feature in the sum spectra is caused by the sensor properties or by the acquisition system. However, the hydrophone and AE ~~data were~~ sensor data were not only captured by different sensors, but they were also acquired with different acquisition systems~~and the sensor types are quite different, this is likely~~. Therefore, it must be concluded that the shape of the sum spectra must be caused by the ~~attenuation~~ properties of the host rock, for example, by the intrinsic attenuation, or the properties of the seismic source. Further analyses, which are beyond the scope of this paper, will be required, to further analyze the frequency spectra.

4 Travel time tomography

Seismic travel time tomography is a well-established procedure for delineating subsurface structures at various scales (e.g., Nolet (1987)). It requires (i) an initial model, (ii) a forward solver to predict the travel times for a given model, (iii) an inverse solver to estimate the seismic velocities (resp. the seismic slownesses, the inverse of velocity) from the observed data, and (iv) a regularization scheme to account for the underdetermined components of the inverse problem (e.g. Menke (1984)). ~~As a forward solver we considered~~ For our computations, we employed an in-house tomography software that included the algorithm by Podvin and Lecomte (1991) as a forward solver, which solves the Eikonal equation on a regular grid with a finite-difference approach. The seismic rays are then computed with a backtracing algorithm ~~(Li et al., 2018).~~ following (Li et al., 2018). The accuracy of the forward solver is governed primarily by the discretization of the finite-difference grid.

To solve the inverse problem, the volume of interest needs to also be discretized in 3D ~~cells of an adequate size. Note that the discretization used for~~ blocks of adequate sizes. In contrast to the forward solver ~~and for the inverse problem do not need~~ grid, which is governed by the accuracy of the Eikonal solver, the inverse grid is governed by the spatial resolution power offered by the source-receiver distribution. Therefore, the forward and inversion grids do not necessarily have to be identical. ~~Then, the~~ The ray segment lengths for each inversion cell and source-receiver pair are determined and fed into the $n \times m$ Jacobian matrix $\mathbf{J}$, where n is the number of data points and m is the number of inversion cells. Since such tomographic problems always include an underdetermined component, regularization of the inverse problem is required. For that purpose, we have added damping and smoothing constraints (see Maurer et al. (1998) and Lanz et al. (1998) for further details). The inverse problem can then be written as

$$\begin{pmatrix}\mathbf{J}\\ \mathbf{D}\end{pmatrix}\mathbf{s}=\begin{pmatrix}\mathbf{t}\\ \mathbf{h}\end{pmatrix}, \tag{1}$$

where $\mathbf{J}$ is the Jacobian matrix, $\mathbf{t}$ the observed travel times, $\mathbf{D}$ and $\mathbf{h}$ the regularization constraints, and $\mathbf{s}$ the unknown slownesses. As described, for example, in Maurer et al. (1998), matrix $\mathbf{D}$ is composed of an upper part, including a $m \times m$ diagonal matrix, which is required for the damping constraints, and a lower part, containing an $m \times m$ matrix, representing the smoothing operator. Likewise, the vector of $\mathbf{h}$ contains an upper part with the initial resp. previous slownesses, and a lower part including zeros. The resulting system of equations in 1 is typically very sparse and can thus be solved conveniently with the LSQR algorithm proposed by Paige and Saunders (1982). With the updated velocity model, the predicted travel times and the ray geometry need to be recomputed to update $\mathbf{J}$. This procedure is then repeated until convergence is achieved.

Since infinitely thin rays, computed with the Eikonal equation, are not a good physical representation of finite-frequency seismic waves, and they often cover not all inversion cells, the concept of fat rays was introduced by Woodward (1992). The underlying idea of this concept is to extend the thin rays to a width that corresponds to the dominant wavelengths of the data observed. When the travel time fields from the solution of the finite-difference Eikonal solver are available, the region of the fat rays can be calculated swiftly with the formula of Červený and Soares (1992) that describe the first Fresnel volume, which is equivalent to the fat ray

$$|t_{sx} + t_{rx} - t_{sr}| \leq T. \qquad (2)$$

t_{sx} and t_{rx} are source or receiver travel times to an arbitrary point x within the forward modeling domain, t_{sr} is the predicted travel time with the actual model $\mathbf{s}$ and T is the dominant period of the seismic waves. When the inequality in Equation 2 is satisfied, the point x lies within the fat ray volume. To compute the fat ray volumes, it is necessary to not only solve the forward problem for each source position, but also for each receiver position, which can increase the computational costs significantly. For computing the fat ray Jacobian matrix, it is necessary to compute for every source-receiver pair a function f_x, defined as

$$f_x = \begin{cases} T - t_{sx} - t_{rx} + t_{sr}, \text{ if } |t_{sx} + t_{rx} - t_{sr}| \leq T \\ \text{0, otherwise} \end{cases} \qquad (3)$$

at every grid point of the forward model. Then, the f_x values, contained in a particular inversion grid cell, are summed up and inserted into the corresponding element of $\mathbf{J}$. Finally, each row of $\mathbf{J}$ needs to be scaled, such that $\mathbf{Js} = \mathbf{t_{sr}}$ is enforced. ~~Husen and Kissling (2001) and Jordi et al. (2016) implemented similar concepts of fat rays for local earthquake tomography and controlled-source tomography respectively~~

It is noteworthy that a fat ray approach makes the tomography less dependent on the parameterization of the inversion model. When a relatively fine block discretization is chosen for the inversion model, it becomes likely that numerous blocks are not hit by thin rays. In contrast, fat rays always cover the same volumes, irrespective of the size of the inversion blocks.

5 Application to field data set

5.1 Setup of the inversion

For the travel time tomography we used the data presented in Section 3. A homogeneous velocity model of 5300 m/s was used as starting model, estimated from travel time curves of our data. Since the geological observations along the main tunnel and

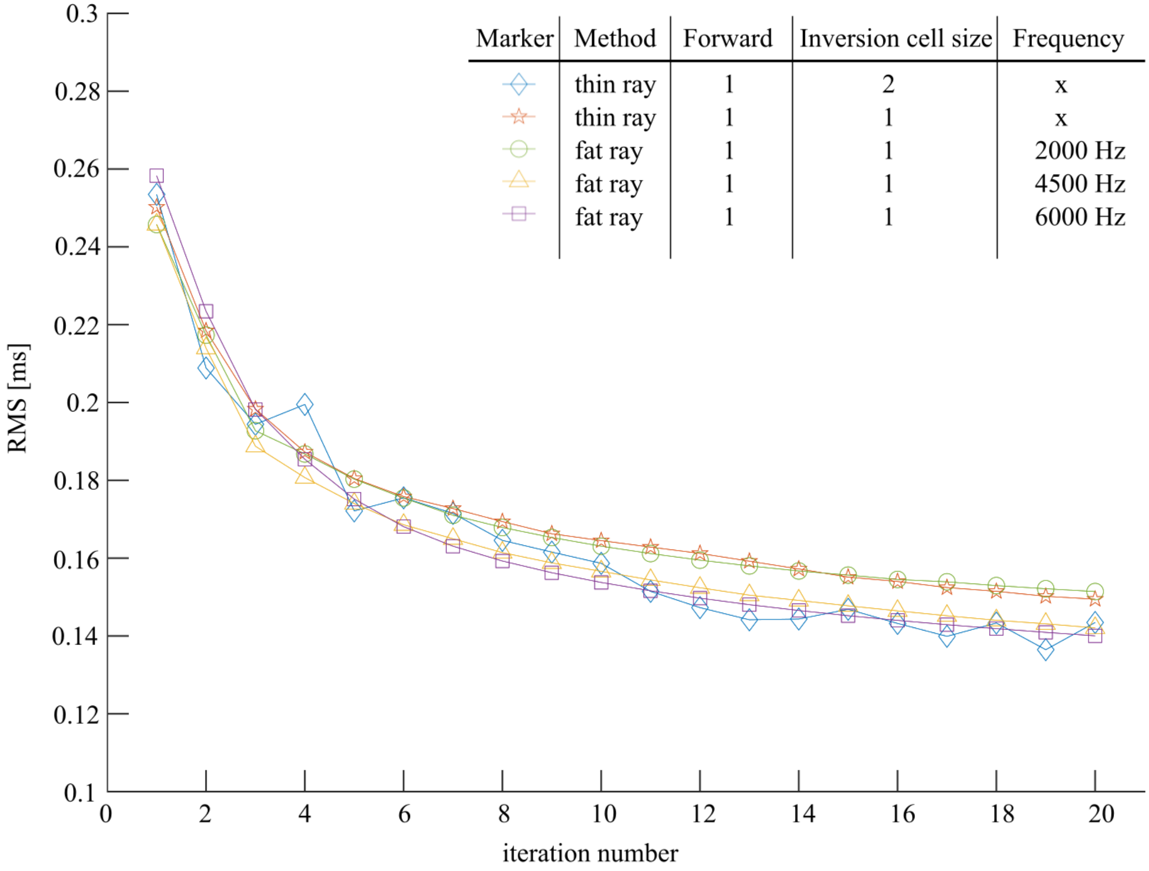

Figure 4. Development of the RMS discrepancy between observed and predicted travel times for different configurations: the thin ray based tomography with two different cell sizes of the inverse solver (1 m and 2 m) and the fat ray tomography with different frequencies, 2 kHz,4.5 kHz and 6 kHz. Fat ray inversions employed the same grid for the forward solution and inversion 1 x 1 x 1 m^3. The same applies to the thin ray 1-1 inversion. For the thin ray 1-2 inversion, 8 forward cells were merged to larger cubic inversion cells.

on the borehole cores did not indicate a pronounced layering, we judged a homogeneous initial model to be adequate. The coordinate system was rotated into the main axis system (or principle axis system) of the borehole trajectories to reduce the number of numerical cells. This resulted in a model of dimension of 72 x 62 x 406 m^3. We compared different ~~cell~~ block sizes for the thin ray-based approach, referred to as "thin ray". The inversion ~~cell~~ block size was either 2 m or 1 m, but the forward solver ~~cell~~ block size was always kept at 1 m.

As described in Section 4, we have applied damping and smoothing constraints for the regularization of the inverse problem. The individual contributions of damping and smoothing were determined by trial-and-error. A damping/smoothing ratio of 0.5 proved to be adequate for our setup.

The convergence behavior of the different inversion runs is shown in Figure 4 in the form of ~~RMS curves~~Root-Mean-Square discrepancies between observed and predicted travel times (RMS curves). For the fat ray tomography, we always used the smaller inversion cell size of 1 m and compared different frequencies: 2 kHz, 4.5 kHz and 6 kHz that are within the frequency spectra of the P-wave (see Figure 3). With appropriate regularization for the different inversions, all inversion runs converged reasonably well, that is, the RMS curves are flattening out, and they all show a similar convergence behavior. However, for the thin ray inversion with 1 m cell size and for the fat ray inversion with 4.5 kHz and 6 kHz, more regularization was required to account for the larger underdetermined component of the inversion problem (the magnitudes of $\mathbf{D}$ and $\mathbf{h}$ in Equation 1 were increased by 50%). Generally, the RMS reduced from 0.25 ms to approximately 0.15 ms within 20 iterations, which is consistent with our picking accuracy. Since we did not observe significant differences in the convergence behavior of the different settings, and the resulting tomography models were similar, we have chosen 2 kHz for our fat ray tomography to obtain the best spatial coverage with the lowest reasonable frequency. ~~An overview of the different slices through the models that we show in this paper, including the MFZ, is shown in Figure **??**.~~

5.2 Comparison of Thin ray and Fat ray tomography

To show the benefit of the fat ray approach, we compare the 2 kHz fat ray results with the thin ray results. For the comparison, we ~~consider the~~ do not only consider the velocity structures, but also the column sums of the Jacobian matrix, subsequently referred to as "coverage", as, for example, described in Jordi et al. (2016). The summation of the jth column of the Jacobian matrix gives an estimate of the overall sensitivity related to the jth inversion cell. The "coverage" measure is similar to the ray-coverage that is often used in thin ray tomography.

In Figure 5, we compare the velocity tomograms for the thin ray (5a) and the 2 kHz fat ray (5b) at ~~150 mdepth~~a horizontal slice at $z = 150$ m. Additionally, the corresponding coverage plots are shown in Figures 5c) and 5d). Higher velocities are displayed in blue, lower velocities in red, and the mean velocity (~~$\approx 5340\,m/s$~~≈ 5340 m/s) is represented in gray. Areas with insufficient coverage are shown in white. The green line indicates the MFZ at this depth. ~~Figure **??** shows an overview of the slice with the boreholes and the MFZ.~~ Both tomograms show similar features, but the structures in the fat ray tomogram (Figure 5b) are much clearer. Note, for example, the low-velocity anomalies around MB8 and between ST1 and ST2. Furthermore, the area, covered with fat rays, is considerably larger, and it does not include any gaps. Considering the fact that ~~the~~ fat rays are a better physical representation of the actual finite frequency wavepaths, one can conclude that the tomogram in Figure 5b is not only clearer, but also likely more reliable~~, and the thin ray tomogram in Figure 5a, which additionally suffers from coverage problems.In the following, we restrict our discussion to the fat ray tomographic model that was computed with a frequency of 2 kHz.~~ .

5.3 ~~3D velocity model~~

5.3 Qualitative description of the 3D velocity model

In the sequel of the paper, we consider only the velocity model obtained with fat ray tomography using a center frequency of 2 kHz. P-wave velocities in ~~the~~ this tomographic model vary between 4685 m/s and 6212 m/s, and the mean velocity is at about 5340 m/s. Figure 6 ~~displays horizontal slices through the final velocity model at different depths. Figure 6~~ shows the tomographic velocities in (a) and the corresponding coverage in (b) at different depths. ~~An overview of the different slices together with the boreholes and the MFZ is given in Figure **??**.~~ The intersections with the boreholes are shown as black dots (a) and blue dots (b), respectively. The intersection of the slice with the MFZ is ~~shown as~~ marked with a green line. ~~There is a conspicuous~~

At $z = 100$ m, we generally observe the highest velocities of all slices. This area is distinguished by largely intact granites (Bröker et al., 2024a). At $z = 150$ m, we observe a low-velocity feature ~~at $z = 150\,m$, which is similar to the feature visible in Figure 5a. Its signature is also weakly visible in the horizontal sliceat $z = 100\,m$, but is absent at $z = 200\,m$. The highest velocities are observed in the slice at $z = 100\,m$~~in the region, where the MFZ intersects the slice. At $z = 200$ m and $z = 250$ m, there are several low- and high-velocity zones with moderate amplitudes. The coverage plots in Figure 6b indicate that all the features described are potentially well constrained by the data (see also Appendix A).

A vertical slice through the model is provided in Figure 7. Since the MFZ (see Figure 1) is a feature of major interest, we provide a vertical section perpendicular to the strike of this fault zone through the central part of the 3D model. The vertical section confirms that there are predominantly low velocities between ~~$z = 100\,m$ to $z = 150\,m$, and uniformly~~ $z = 100$ m to $z = 150$ m, and generally higher velocities are observed at greater depths ~~. Below $z = 250\,m$~~(see, for example, the region marked with an arrow in Figure 7). Below $z = 250$ m, the coverage and thus the reliability of the velocity model is ~~very low~~limited.

The horizontal and vertical slices in Figures ~~5~~ 6 and 7 provide some insights into the structure of the 3D velocity model. However, such single slices can be difficult to interpret. Therefore, we have created a series of videos, with which it is possible to scan in various directions through the model cube. They are provided in the digital appendix, and it is highly recommended to make use of them to better understand the structures contained in the 3D model.

The horizontal and vertical slices in Figures 6 and 7 indicate that there are hints of the MFZ (e.g., the low-velocities near the MFZ intersection at $z = 150\,\mathrm{m}$ in Figure 6), but there is no consistent manifestations of it in the 3D velocity. This can either be indicative for a high degree of complexity of the MFZ, but it could also be due to insufficient spatial resolution of the tomograms. To address the latter, we have performed a series of checkerboard tests that are documented in Appendix A. In brief, the tests demonstrated that the spatial resolution lies between 5 and 10 m, with decreased resolution towards the borders of the regions with significant coverage.

5.4 ~~Validation of the velocity model with independent data sets~~Travel time residuals

To check, how well the 3D tomographic velocity model is capable to explain the observed travel times, we superimpose the observed and predicted travel times in Figure 8a as a function of source-receiver offset. For a better visualization, the travel times t_{eff} are shown in reduced form, that is, $t_{red} = t_{eff} - \Delta/v_{red}$, where Δ is the source-receiver offset and v_{red} is the reduction velocity, which we have chosen to be 5340 m/s . Consequently, travel times with a ray velocity of v_{red} plot along a horizontal line at $t_{red} = 0$. Additionally, we show the differences between the observed and predicted data (residuals) a function of source-receiver offset (Figure 8b) and in form of a histogram (Figure 8c).

From the residual plots in Figure 8, two main conclusions can be drawn. First, there seem to be no significant offset dependent variations of the residuals (such variations could be indicative for systematic errors in the tomograms). Secondly, about 70% of the residuals are below the average picking accuracy of 0.15 ms (marked with solid black lines in Figures 8b and 8c). Therefore, the standard deviation of the residual distribution is close to the average picking accuracy, thereby indicating that the observed data are neither over- nor under-fitted by the 3D tomographic velocity model.

5.5 Validation of the velocity model with independent data sets

Laboratory measurements at fluid-saturated undisturbed core samples indicated values up to V_p=5434 m/s. From these results, P-wave velocities at in-situ conditions with P_{eff}=15 MPa were estimated to be 6123 m/s (David et al., 2020). This is broadly consistent with the maximum values observed in the tomograms (6212 m/s).

Another option to validate the velocities obtained by the tomographic inversions is offered by sonic logs, acquired in borehole ST1. A comparison is shown in Figure 9. To compare both ~~datasets~~data sets, the sonic logs were downsampled to the sampling rate of the tomographic velocity model. The tomographic velocities are shown in black ~~, those from~~ and those from the sonic logs in orange. Adjacent to the velocity profiles, we have also extracted the coverage values along ST1, shown as blue line. They show that the depth range of trustworthy tomographic velocities lies between 50 m and 230 m (denoted by horizontal dashed lines in Figure 9. As a consequence, the tomographic velocities above and below the depth range resolved are close to the initial velocities of 5300 m/s.

~~In the depth range resolved~~

In the resolved depth range, the sonic logs show slightly higher velocities compared with the tomographic results. This is expected because the sonic logs employ higher frequencies. Therefore, the comparison with the sonic logs is rather restricted to relative velocity changes. Both curves show a significant low-velocity anomaly at about 150 m depth. To verify this low-

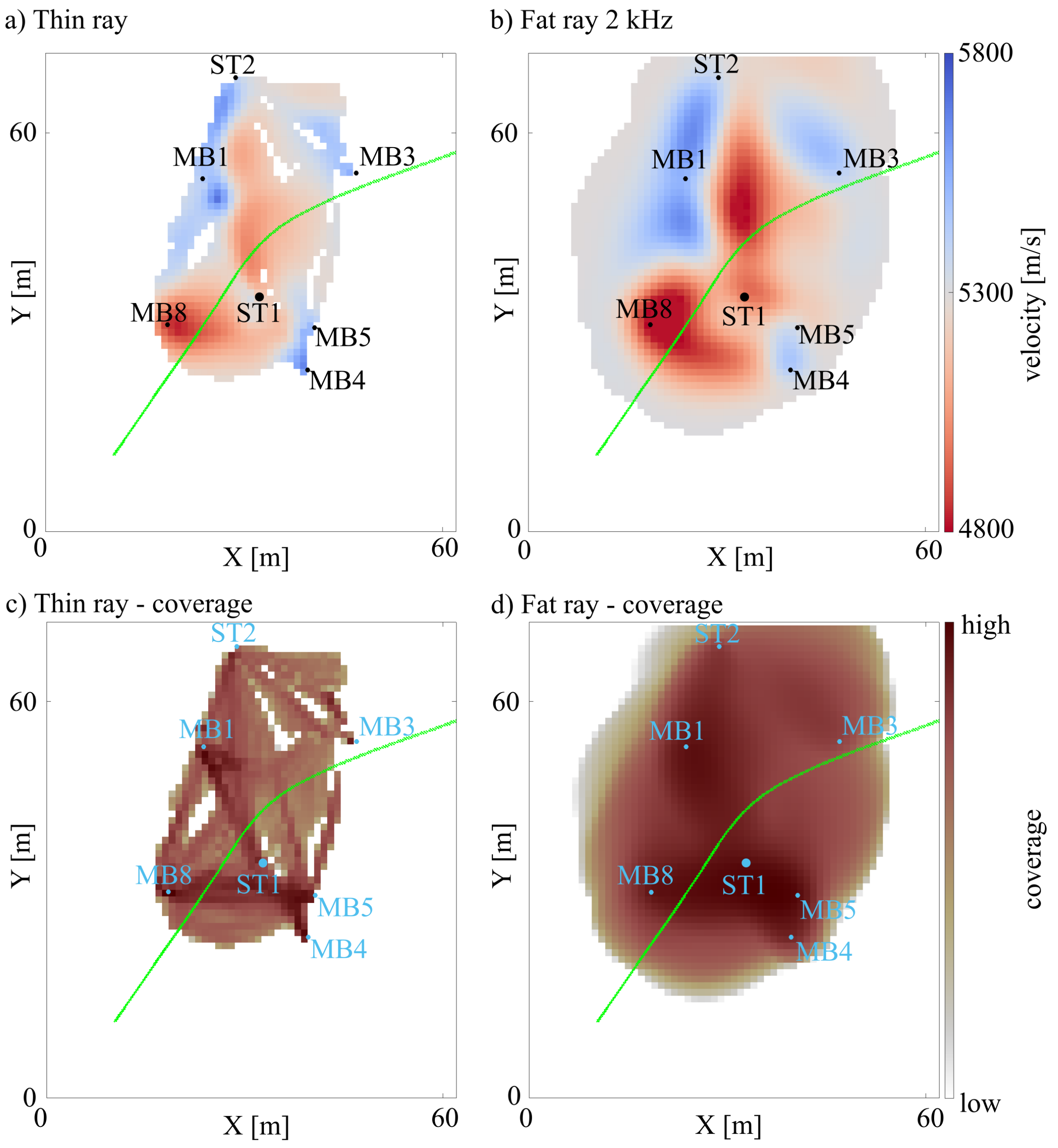

Figure 5. ~~Overview~~ Comparison of ~~the different slices that are shown in Figure 5 (~~thin and fat ray tomography using a x-y slice at ~~150~~ $z = 150$ m: a) tomogram of the thin ray approach, ~~Figure 6 (slices at 100 m, 150 m, 200 m and 250~~b) tomogram of the 2 ~~m~~kHz fat ray approach. The intersections of the boreholes with the slice are also shown. (c) and ~~Figure 7 (slice perpendicular to the MFZ~~d) show the coverage, defined via the column sums of the Jacobian matrix.

~~Tomograms of the final velocity model in x-y-plane at $z = 150\,m$: (a) tomogram of the thin ray approach, (b) tomogram of the 2 kHz fat ray approach. Unresolved areas are left white. The dots indicate the intersections of the boreholes with the slice at $z = 150\,m$, while the larger dot indicates the borehole ST1. The upper tomograms show the velocities, the lower one show the corresponding coverage of the model. The green line shows the intersection of the MFZ with the x-y-plane at 150 m.~~

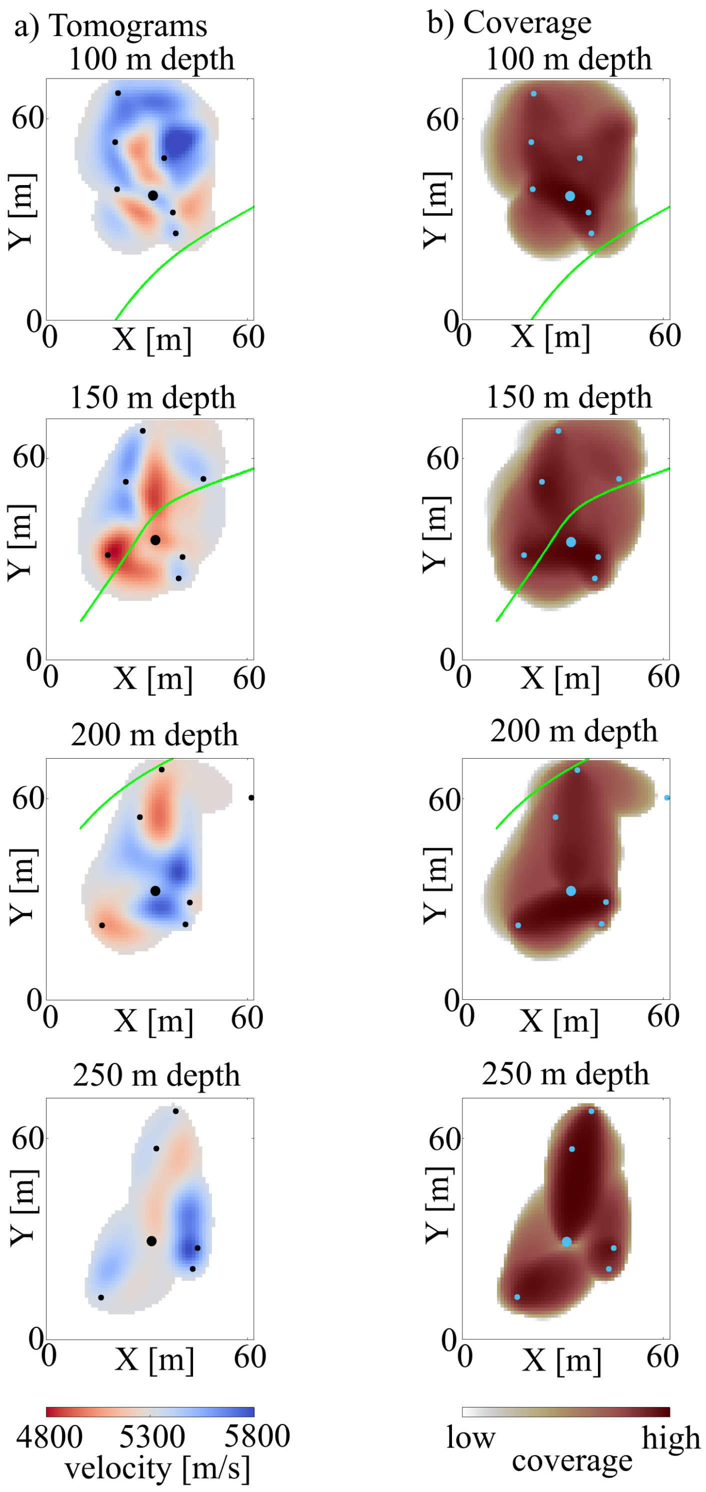

Figure 6. a) Velocity tomograms at different depths and b) the corresponding spatial coverage~~in b)~~. Unresolved areas are left white. The dots indicate the intersections of the boreholes with the slice, the larger dot indicates the borehole ST1. The green line indicates the intersection with the MFZ.

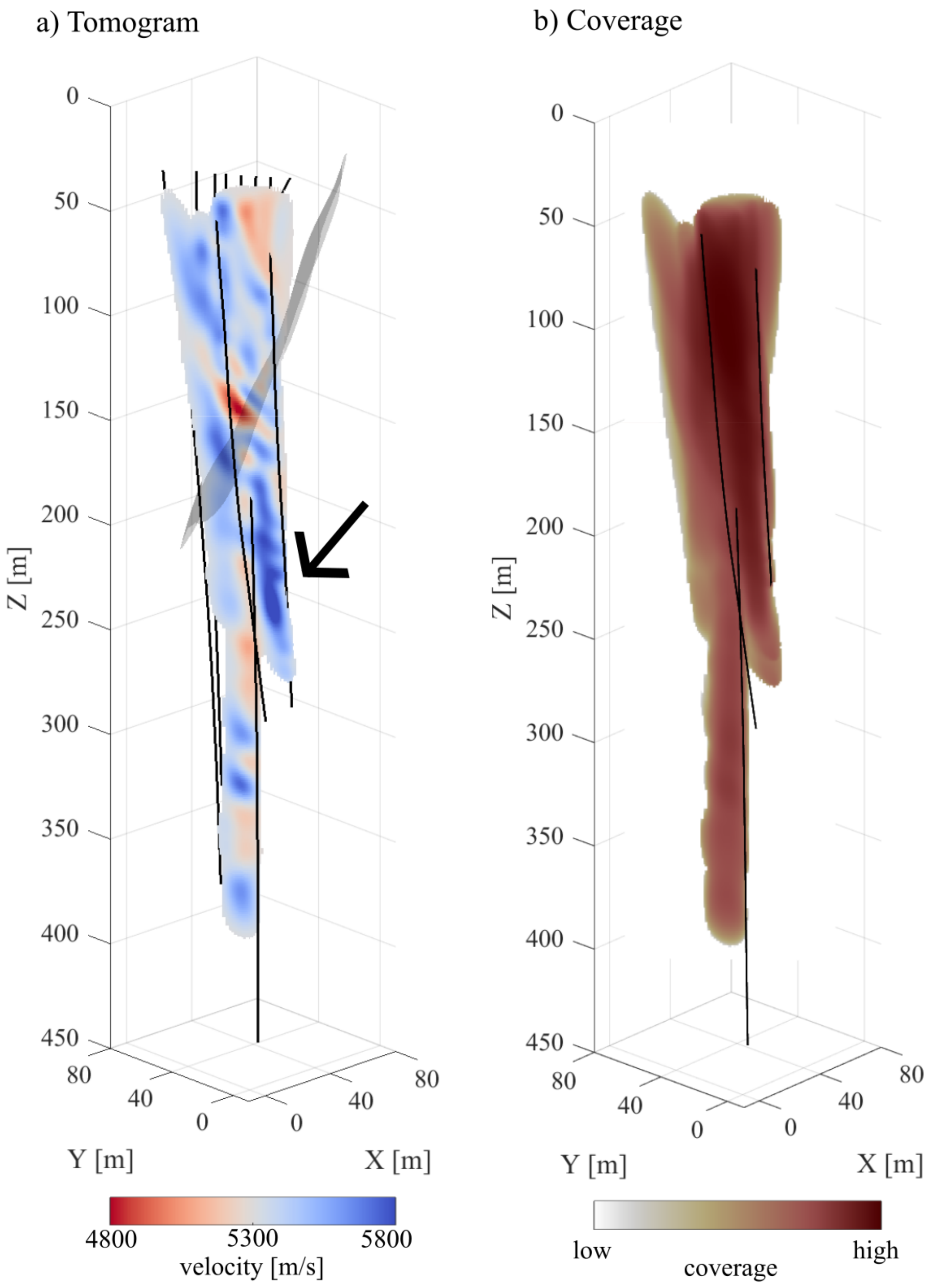

Figure 7. a) ~~shows a tomogram~~ Vertical slice perpendicular to the ~~fault zone~~ MFZ, which is shown as gray surface~~(data from GPR measurements (Escallon et al., 2024))~~. Zone with particularly high velocities is marked with an arrow b) shows the same slice but for the coverage of the model.~~It shows, that the coverage is good between 50 m to 230 m but with a linear shape. The linearity of the low-velocity zone with the depth direction might be caused by lower coverage at the edges of the model.~~

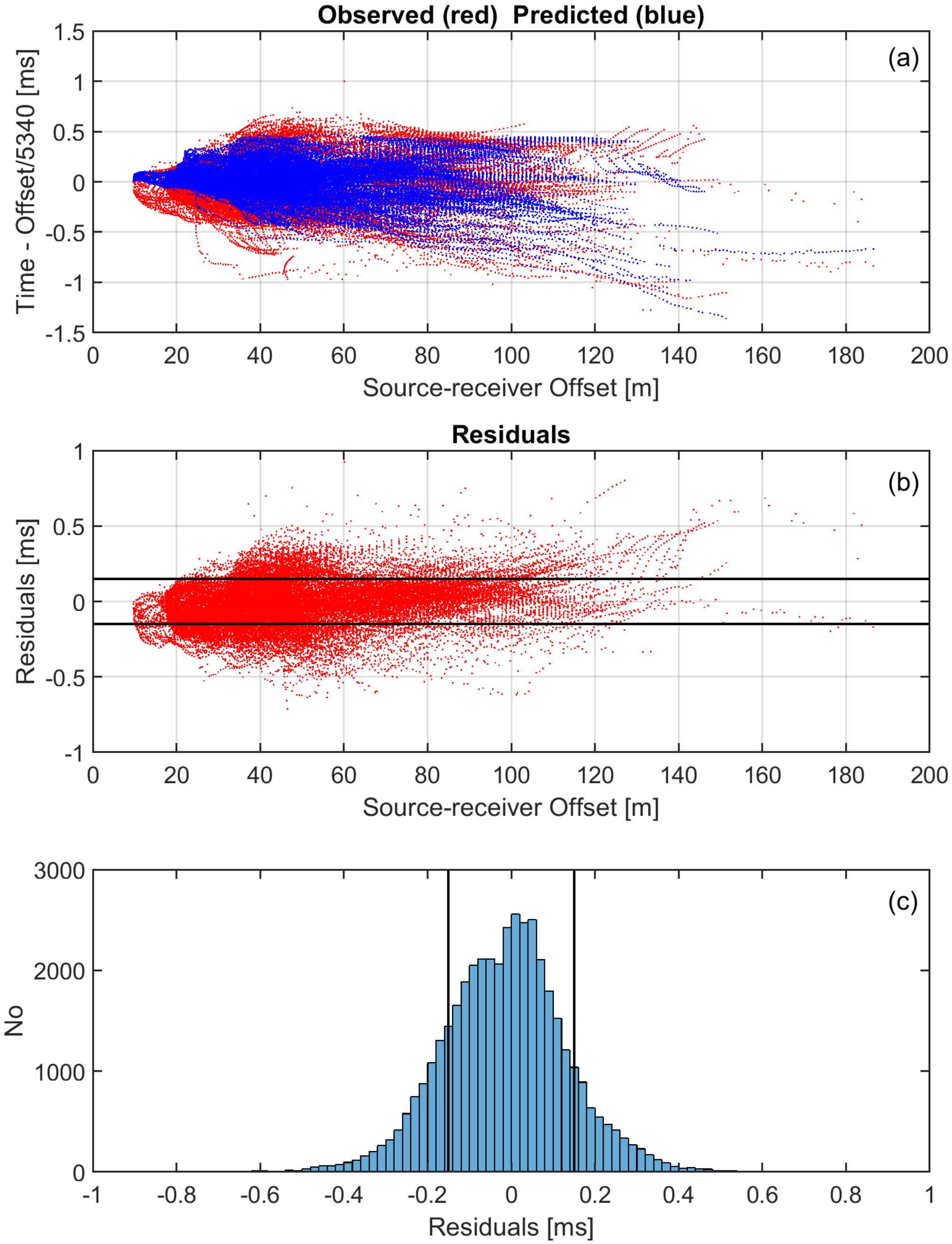

Figure 8. (a) Observed (red) and predicted (blue) travel times as a function of source-receiver offset. (b) Corresponding residuals plotted as a function of source-receiver offset. (c) Residuals shown in form of a histogram. The manually determined picking accuracy is indicated with solid black lines in (b) and (c).

velocity zone as a feature of the MFZ, we compare it with ATV (Acoustic Televiewer Log) measurements (Figure 9, right panel) at this depth. We show the ATV travel ~~time~~times, adapted from ~~?~~Bröker et al. (2024a). The ATV measurements reveal a broad fracture zone shown by an increase in ATV travel time up to 180 μs. ~~A more detailed analysis of the borehole cores is shown in ? e.g. Figure 3). They compare different borehole logs from ST1 and concluded that temperature, conductivity, spinner up and ATV logs all show a prominent structure in Unit 3 indicated as "Largest fracture zone". The different geological measurements show a variety of smaller breakoutsand fractures. However, it seems that the tomographic velocities are mostly sensitive to the MFZ~~Furthermore, Bröker et al. (2024a) provide more evidence on the existence of a significant fracture zone. Spinner, electrical conductivity and temperature logs exhibit very significant anomalies in this depth range. Furthermore, optical televiewer measurements indicate smaller breakouts.

~~The comparisons~~

The velocities of the 3D seismic model~~with the borehole logs and borehole cores shows a generally good agreement along~~, extracted along borehole ST1, generally show a good agreement with the borehole logs. So the question arises, if the ~~tomographically derived velocity structures~~ tomographic velocity model would allow delineations and characterizations further away from the boreholes, where no ground truth information is available. For that purpose, we ~~compare the tomographically derived velocities with the geometry of the MFZ, as derived by Escallon et al. (2024). In~~ consider again the horizontal and vertical slices through the 3D velocity model (Figures 6 and 7 ~~, the MFZ structure is superimposed~~and the movies provided in the digital appendix). If the MFZ would be a clearly confined zone, one would expect a correspondingly well-confined low-velocity zone in the velocity model. Instead, we observe generally decreased velocities along the MFZ ~~traces~~intersections, but there is also a substantial amount of heterogeneity. ~~This may be partially the result of the limited spatial resolution power of the tomograms, but it most likely indicates that the MFZis a complex faulting structure, affecting larger volumes of the host rock, and including substantial heterogeneities~~At the horizontal slice at $z = 150$ m (Figure 6), the MFZ is crosscutting the slice in its central part, where the spatial resolution is best, but at $z = 100$ m and $z = 200$ m, the intersection is at the border of the resolution limit (Figure 6b). As demonstrated in Appendix A, the resolving power of our data set is limited towards the edges of the regions with coverage. Therefore, it remains unclear, if the heterogeneities are the result of the complexity of the MFZ, or if they are caused by the limited spatial resolution. Most likely, both effects contribute to the velocity structures observed.

5.6 Appraisal of rock quality

The velocity variations found in the tomographic volume are relatively small, and 99% of the velocities lie in the range ~~$4900 < v_p < 5800 m/s$~~$4900 < v_p < 5800$ m/s. This is consistent with the findings from borehole logs (Shakas, 2019) that the host rock is moderately disturbed. The velocity variations can be further quantified using the seismic rock quality designation factor (SRQD) introduced by Deere and Miller (1966):

$$SRQD = \left(\frac{v_p}{v_p^{lab}}\right)^2 \times 100. \tag{4}$$

v_p^{lab} is the velocity of the intact rock measured in the laboratory, which is ~~$6123 m/s$~~ 6123 m/s for the BedrettoLab (David et al., 2020). According to Deere and Deere (1988), the SRQD is a good approximation to the rock quality designation

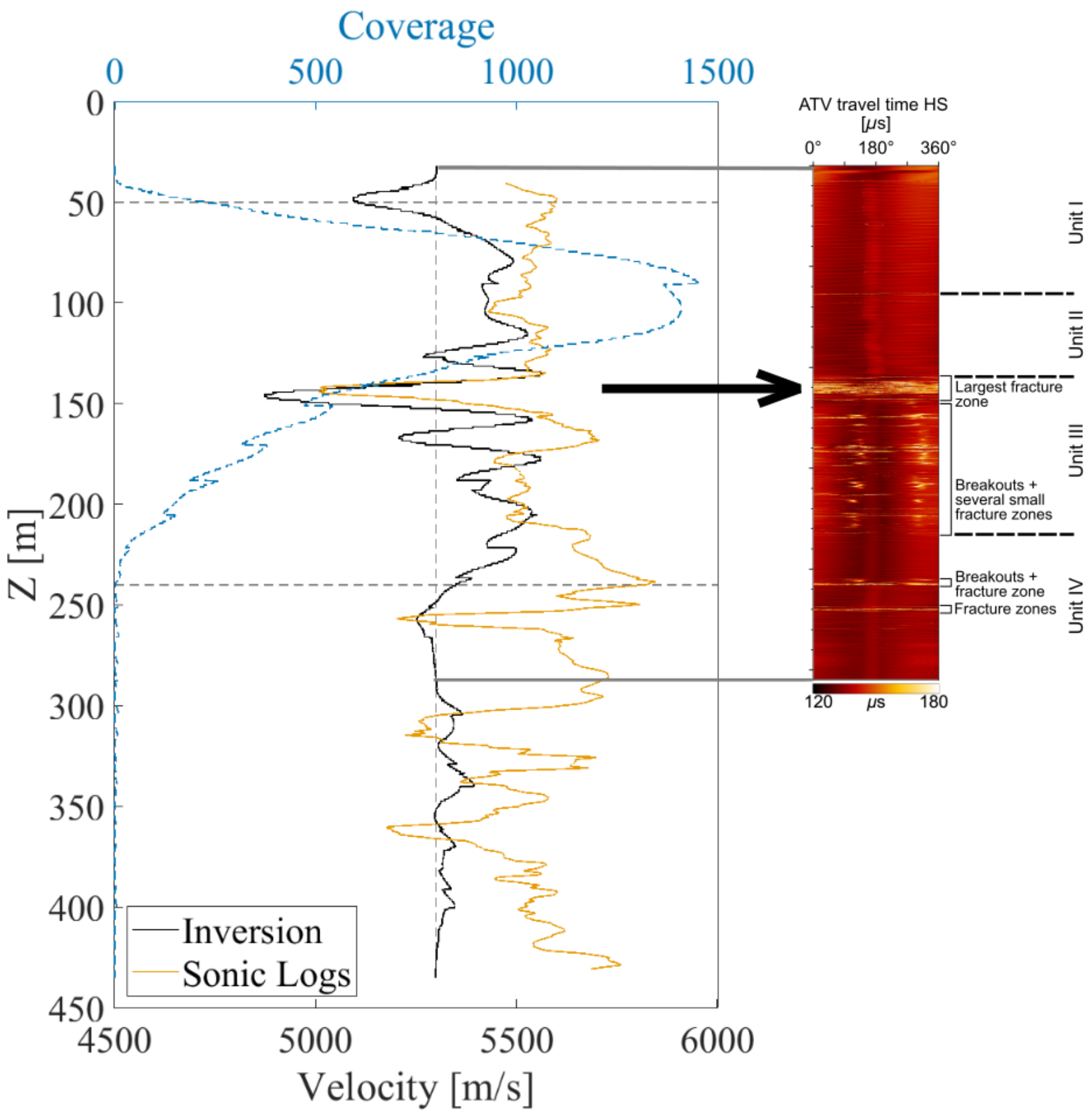

Figure 9. Comparison of the inversion results with ~~geological~~ additional data ~~. For this purpose,~~ acquired along the ~~tomographic velocities~~ central borehole ST1 (~~black line~~Figure 1)~~are~~ . Tomographic velocities, extracted along ~~the borehole~~ ST1 (~~in the middle of the volume~~black) ~~and~~ are compared ~~to the~~ with sonic ~~logs~~ log data (orange~~line~~). The ~~coverage along ST1 is shown in blue. The~~ horizontal gray dashed lines indicate the zone of ~~reasonable good~~ significant coverage ~~,~~ shown with a dashed blue line (between ~~50~~ $z = 50$ m and ~~250~~ $z = 250$ m~~depths~~). ~~We~~ In this range, we compare the results with ATV logs ~~(on the right)~~ from ~~ST1, which show a fractured zone, that match the low-velocity zone. For the ATV's we adjusted Figure 3 from ? such that the depth is matching the inversion coordinate system used in this paper~~Bröker et al. (2024a)

.

factor (RQD). The SRQD values within our tomographic model lie between 64 and 90, which translates to a rock quality from "fair" to "good/excellent" (Deere and Deere, 1988). This is consistent with geological observations in the geothermal testbed~~(Ma et al., 2022)~~ . Based on tunnel observations and borehole logs, Ma et al. (2022) concluded that the general amount of fracturing in the geothermal testbed is low to moderate.

5.7 Limitations of the tomographic velocity model

For an appropriate interpretation of the structures found in the tomographic 3D model, it is necessary to consider its inherent limitation. First of all, the spatial resolution needs to be considered. It is influenced by the ray coverage within the model and the seismic wavelengths. As shown in Figures 6 and 7, the coverage of the fat rays is generally high and homogeneous. Williamson and Worthington (1993) demonstrated that the spatial resolution scales approximately with the width of the Fresnel zone. For a frequency of 2 kHz and an average source-receiver distance of about 50 m, the width of the Fresnel zone is approximately 10 m, which corresponds quite well with the minium feature size in the fat ray tomograms. Furthermore, this is remarkably consistent with the results of the checkerboard tests documented in Appendix A.

Further factors that may limit the reliability of the tomograms include the presence of seismic anisotropy and accuracy of the borehole traces. As ~~already~~ indicated earlier, minor anisotropy effects may exist, but we have chosen to employ an isotropic model. Ignoring significant anisotropy effects during an isotropic inversion would result in layered structures with alternating high and low velocities, thereby mimicking anisotropy. We did not spot a pronounced layering in our tomograms.~~Similarly, in the presence of significant borehole trace errors , one would expect velocity anomalies towards the bottom~~

Another potential source of systematic errors includes inaccuracies of the borehole trajectories, which tend to increase towards the bottoms of the boreholes. Maurer and Green (1997) has shown that such deviations from the true trajectories would result in substantial anomalies near the borehole bottoms, where the formal resolution is worst and anomalies, caused by systematic errors, can develop most easily~~(Maurer and Green, 1997). Again such~~ . Such effects are not observed in our tomograms.

Although we can exclude major artifacts from systematic errors, introduced by anisotropy and borehole ~~trace~~ trajectory inaccuracies, it cannot be excluded that they may have introduced minor distortions. Therefore, only gross features in the tomograms should be interpreted.

5.8 Comparison of seismic velocities with ~~acoustic emission (AE) events~~induced seismicity

In 2022 ~~and~~ - 2023, ~~several~~ hydraulic stimulation experiments were conducted in the geothermal testbed ~~. The stimulations were performed~~ by injecting water ~~in~~ into selected packer intervals of borehole ST1 (see also Section 2). An overview of these experiments ~~in the context of induced seismicity is presented in Obermann et al. (2024). The analysis was performed with DugSeis (Rosskopf et al., 2024b), and more details are provided in Rosskopf et al. (2024a). The stimulations were subdivided~~

~~in several phases. We restrict ourselves to events recorded during Phase I. In this phase, eight intervals in the range of $121.1 < z < 299.54\ m$ were stimulated in a consistent manner with similar injection protocols (**?**Doonechaly et al., 2024)~~ is given in Obermann et al. (2024), with a seismic analysis using DugSeis (Rosskopf et al., 2024b, a). We focus here on the seismicity from Phase I, in which eight intervals at depths of $120 < z < 300\ m$ were stimulated using consistent injection protocols (Bröker et al., 2024a; Doonechaly et al., 2024). We examine the relationship between seismicity and our 3D tomographic velocity model, and assess the effect of velocity heterogeneity on location accuracy.

~~For our analyses, we started with the so-called HQ (high quality) events , as described in Obermann et al. (2024). We then restricted our selection to those events lying~~

For the analysis, we selected well-constrained events from the catalog of Obermann et al. (2024), restricted to those within the tomographic model. ~~Subsequently, we applied an additional filtering by selecting events that (i) had at least 6 reliable P wave picks (i.e., with corresponding residuals ≤~~ Events required at least six P-wave picks (no S-wave picks were available) and were relocated using a grid-search algorithm (Moser et al., 1992) with travel times computed via the Eikonal solver (Podvin and Lecomte, 1991) on a 0.5 m grid. Outliers in the pick database were removed using a 0.75 ms ~~), (ii) an RMS misfit of less than 0.5 ms (iii) a determinant of the corresponding Jacobian matrix of more than $1e^{-7}$ (essentially~~ threshold, after which the selection criteria were re-applied and events re-relocated. We further excluded events with poor location geometry using the D-criterion ~~used by Kijko (1977) . This selection procedure left~~ (Kijko, 1977; Menke, 1984), adopting a threshold of 1×10^{-7} based on visual inspection. This procedure yielded 4283 events ~~that were considered~~ from originally 6413 events for further analysis.~~The selected events were finally relocated using the 3D tomographic model, presented in this study, and a grid-search location algorithm similar to the methodology described in Moser et al. (1992). For that purpose, we upsampled the velocity model to a grid spacing of 0.5 m.~~

~~In~~

All considered events have moment magnitudes $M_w < -3$ and can therefore be attributed to the fluid injections within the geothermal testbed, excluding regional seismicity. Crosshole measurements were performed prior to injection and thus represent pre-stimulation conditions. Since repeated active measurements during stimulation indicated P-wave velocity changes well below 1%, this has negligible impact.

5.8.1 Influence of the velocity model on hypocentral parameters

Figures 10 and 11 ~~, the effects of the 3D model on the locations are illustrated. We located the events~~ compare event locations obtained with the 3D tomographic model and a homogeneous velocity model with the average velocity ~~(~~of 5340 m/s~~)~~ , both using the same grid search algorithm~~, and analysed the differences. The histogram in Figure 10 demonstrates that most differences are rather~~ . Differences are generally small (mean~~difference~~: 2.2 m, median~~difference~~: 1.4 m), ~~and the spatial distribution of the differences in Figure 11 indicate that the effects of the 3D model tend to be slightly more pronounced at $z > 220 m$. It is also noteworthy that there is no systematic shift between the two location algorithms. From these observations we conclude that the effect of~~ with slightly larger deviations at depth $z > 210$ m. No systematic shift is observed between the event locations using the two velocity models. We therefore conclude in line with observations from Rosskopf et al. (2024a) that velocity

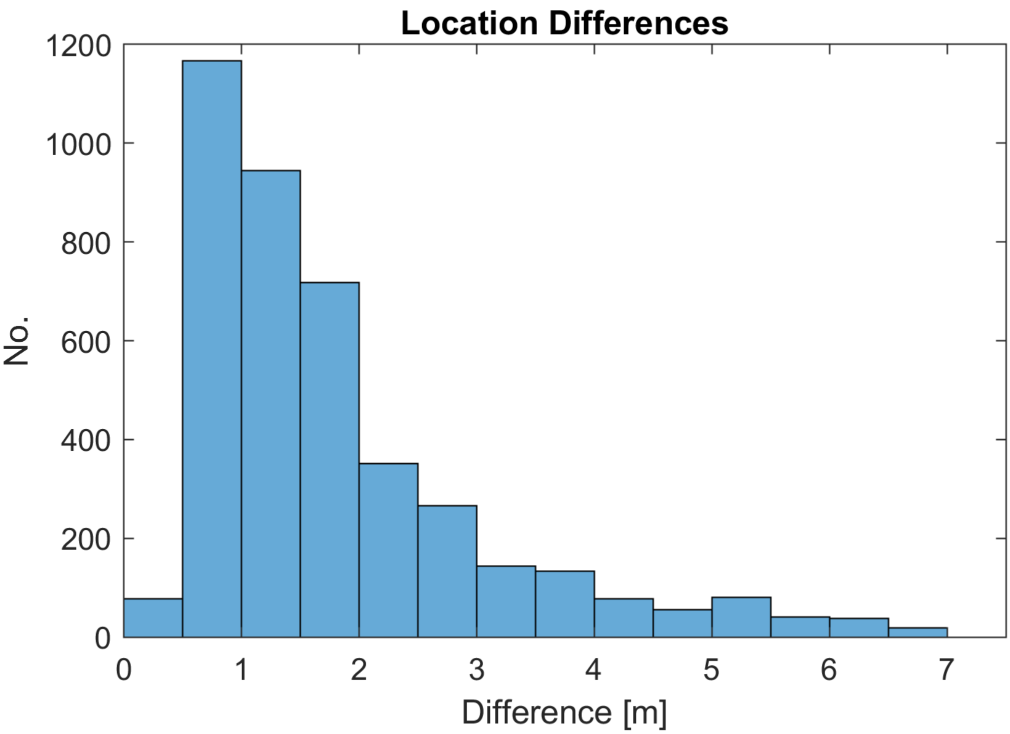

Figure 10. Histogram of the absolute location differences using either a homogeneous or the 3D tomographic model.

variations in the 3D model ~~on the hypocentral locationsis quite minor, which is in agreement with the investigations of Rosskopf et al. (2024a)~~have only minor effect on event locations.

~~However, it is interesting to consider~~

5.8.2 Spatial correlation of seismic velocities and the induced seismicity

To study the spatial correlation between ~~the seismic activity and the seismic velocities. For that purpose, we subdivide~~ seismicity and velocity structures, we employed the following methodology. First, we subdivided the velocity model into low-, intermediate and high-velocity regions~~, and compare them with the predominant locations of the seismicity~~. Low and high ~~velocity regions~~ velocities are defined as ~~zones, in which the velocities are either lower or higher~~ values more than one standard deviation (~~$\approx 150\,m/s$) from~~ ≈ 150 m/s) below or above the mean velocity (~~$\approx 5340\,m/s$)of the resolved areas within the 3D tomogram. For the analysis, we consider horizontal slices through the region of interest, as well as a vertical slice approx. perpendicular to the MFZ. For each slice , we superimpose the seismic events that have occurred on or near ($\pm 2.5\,m$) the slices . The results are shown in~~ ≈ 5340 m/s). Then, seismic events were superimposed on horizontal and vertical slices of the velocity model, within ± 2.5 m of each slice (Figures 12 and 13~~, and movies, showing all horizontal and vertical slices, are~~

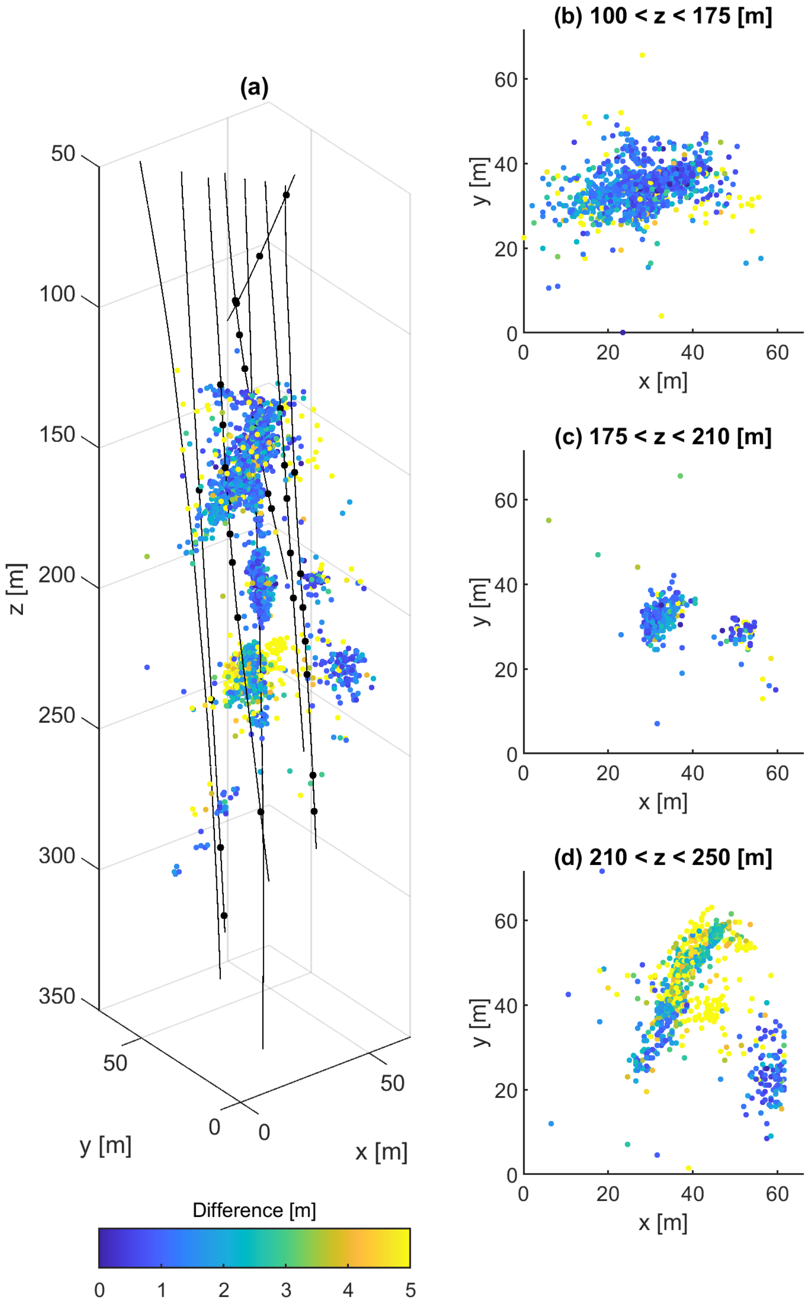

Figure 11. Spatial distribution of location differences shown in Figure 10. Panels (b) to (d) include top view representations of selected depth intervals.

~~provided~~ ; full slice series in the digital appendix).

~~We observe a conspicuous correlation between the seismicity and the velocity pattern. The seismic events seem to "avoid" the high velocity (blue) regions, and they occur rarely within the regions of very low velocities (dark red). The majority of the events can be found in the regions of intermediate and slightly decreased velocities (grey and light red), and some of the slices show a remarkable event clustering along the boundaries between intermediate and high velocities (e.g. , Figure 13b). A deviation of this correlation is found in areas near the injection borehole~~

Several interesting observations can be made in the superimposed images in Figures 12 and 13. In horizontal slices at injection depths seismicity clusters around the injection borehole ST1, with little correlation to the MFZ (green lines in Figure 12). Most events occur in slightly reduced or intermediate velocity zones and only very rarely in high- or very low-velocity regions. At $z = 237\,\mathrm{m}$, a distinct cluster lies about 20 m from ST1~~(marked red in Figure 12). Here, the AE activity is tightly coupled with the injection process itself~~, almost entirely in the intermediate velocity range. Vertical slices show similar patterns (Figure 13): events are concentrated in slightly reduced or intermediate velocity zones, often along boundaries towards higher-velocity regions.

~~A rather qualitative~~

A possible interpretation of these ~~observations could be as follows. High velocity areas represent~~ patterns is that high velocities correspond to intact host rock ~~, and the~~ that remained unfractured under injection pressures (~~up to approximately~~ $<$ 18 MPa)~~were apparently insufficient to break up these areas. Very low velocities may represent considerably fractured zones , where it is no longer possible to accumulate sufficient stresslevels, such that significant seismic activity can occur. In intermediate velocity regions, pre-existing fractures may exist , but the rock strength is still high enough, such that~~ , whereas very low velocities indicate heavily fractured zones incapable of storing sufficient stress. Seismicity thus preferentially occurs in intermediate zones, where fractures exist but rock strength still allows stress accumulation and ~~subsequent break-up can occur. It should be noted that the crosshole measurements were performed prior to the injections, and represent thus the state prior to the injection experiments. However, this is of minor importance, since we expect only very minor velocity changes caused by the injections. Initial analyses of repeated active seismic measurements during the stimulation experiments indicated that the expected velocity changes are well below 1 % . For a more detailed interpretation, we consider the relationship between seismic velocities and mechanical stiffness, which are linked through elasticity and continuum mechanics (e.g., Mavko et al. (2009))~~failure.

From a mechanical perspective, seismic velocities reflect stiffness. Microcracking and pore fluids ~~significantly influence these velocities (e.g. Paterson and Wong (2005)). Damage, characterized by microfracturing, is a key indicator of brittle deformation in geological settings, extensively documented in natural fault zones (e.g. Faulkner et al. (2010), and references therein). Laboratory rock failure tests demonstrate that increased microcracking reduces wave speeds and stiffness (e.g. Stanchits et al. (2011)).The variation in stiffness , inferred from seismic velocities, likely produces strain gradients between the slower, damaged material and the stiffer, intact~~ lower velocities and stiffness (e.g., Mavko et al., 2009; Paterson and Wong, 2005), consistent with fault-zone observations (e.g., Faulkner et al., 2010) and laboratory rock-failure experiments (e.g., Stanchits et al., 2011) . Velocity contrasts likely create strain gradients and stress concentration at boundaries between intact and damaged rock -

a mechanism invoked for acoustic emissions in granite (Salazar Vásquez et al., 2024) and rock ~~matrix during fluid injection tests. The strain gradient reflects, how the deformation will vary throughout the body, resulting in stress concentrations over the velocity gradient. This mechanism has explained the patterns of AEs in the Rotondo granite in laboratory test (Salazar Vásquez et al., 2024) and has also been proposed to explain rock bursts around the EDZ in mining environments (Barton, 2006)(Chap. 7.2)~~bursts in mines (Barton, 2006).

A complementary mechanism ~~for the AEs produced in the medium and lower velocity zones is that permeability increases with the presence of connected microcracks and damage. The lowerand medium velocity regions present preexisting higher permeability zones. During fluid injection, the pore fluid pressure will migrate preferentially into these regions. If these regions have preexisting structures that are preferentially oriented and close to failure, only small fluid pressure perturbation would be needed to induce failure~~ is fluid migration: lower/intermediate velocity regions are more permeable due to connected microcracks. Fluid preferentially infiltrates these zones, where small pressure perturbations can induce failure if structures are near critical stress (Townend and Zoback, 2000).

~~It is remarkable that similar observations were made in the laboratory (i.e., centimeter scale, (Salazar Vásquez et al., 2024)) and within our geothermal testbed (decameter scale), and it is even more interesting to note that similar observations can also be made at larger scale. Local earthquake tomography investigations in the Hengill geothermal field (kilometer scale) (Obermann et al., 2022)also show a clustering of the seismic events in zones of intermediate velocities. Therefore, it seems that the underlying mechanisms are pretty much scale independent~~

We finally checked, if similar correlations between seismicity and intermediate velocity zones have been observed at other places and across scales. As already mentioned, they were observed in centimeter-scale laboratory tests Salazar Vásquez et al. (2024) , and similar observations were made at kilometer-scale geothermal fields (e.g. Hengill, Iceland (Obermann et al., 2022)). Therefore, we conclude that the spatial correlation of seismicity and intermediate velocity zones at the BedrettoLab geothermal testbed is consistent with other observations across scales. The most plausible explanations involve stress gradients at velocity contrasts and enhanced permeability in fractured zones. Further work is needed to quantify these mechanisms and link observations with geomechanical processes more directly.

6 Conclusions

The experimental setup of the geothermal testbed in the BedrettoLab offered unique opportunities for 3D tomographic studies. The literature on such investigations on that scale is very sparse - in fact, we could not find a comparable study in the literature. Our finding could thus be a motivation for other experiments in similar environments.

~~We can clearly show~~

We showed that in comparison with traditional thin ray methods, fat ray tomography does not only better mimic the physics of band-limited seismic data, but it also results in an improved coverage. ~~It is also worthwhile mentioning that~~ Furthermore, fat ray tomography is less dependent on the model parametrization of the ~~forward and inversion grids~~ inversion grid (compared

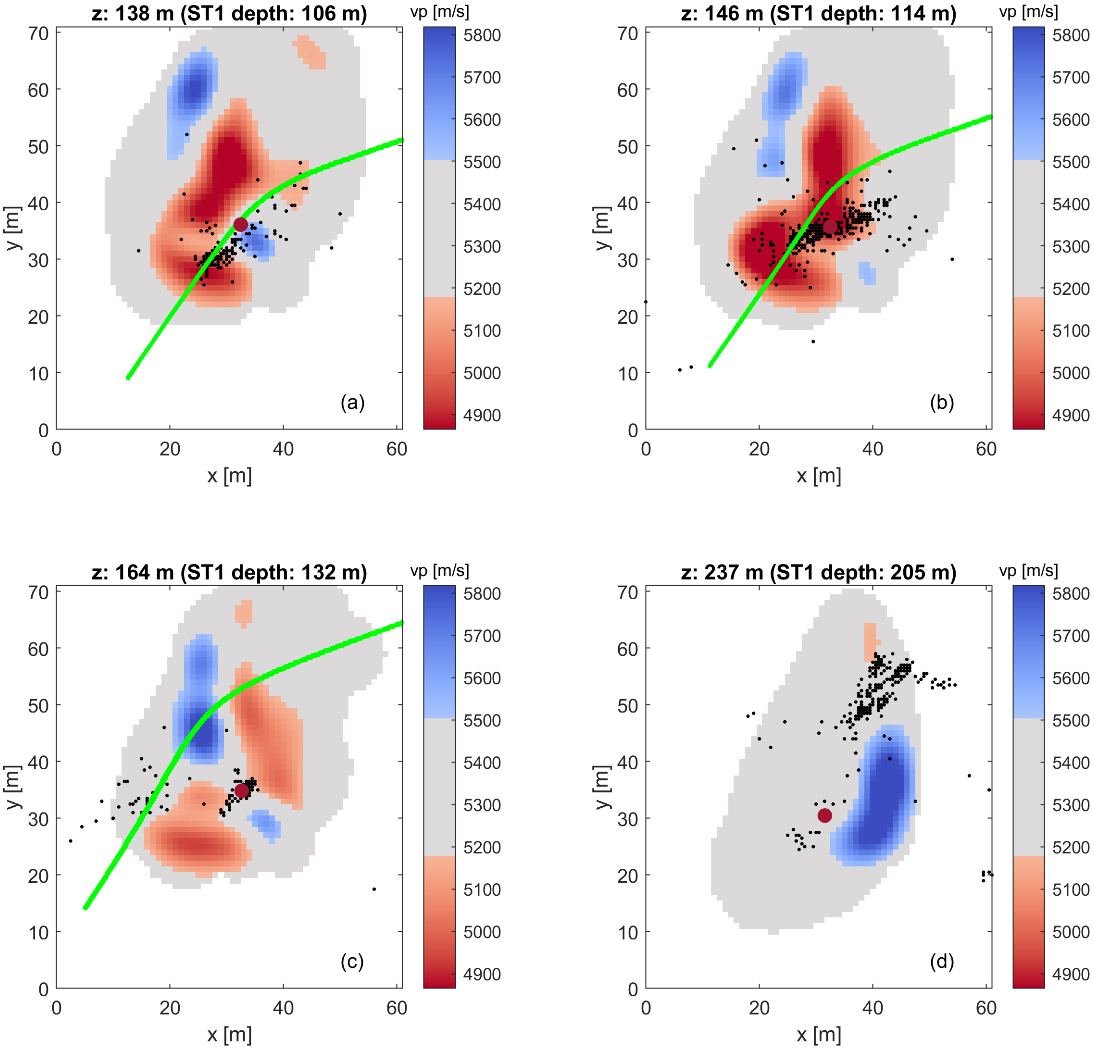

Figure 12. Horizontal slices through the tomographic model. Low and high velocities are shown in red and blue, and intermediate velocity areas are shown gray. The seismicity located ~~±2.5 *m*~~ ±2.5 m distance from the slices is superimposed by black dots. The intersection of the MFZ is shown in light green.

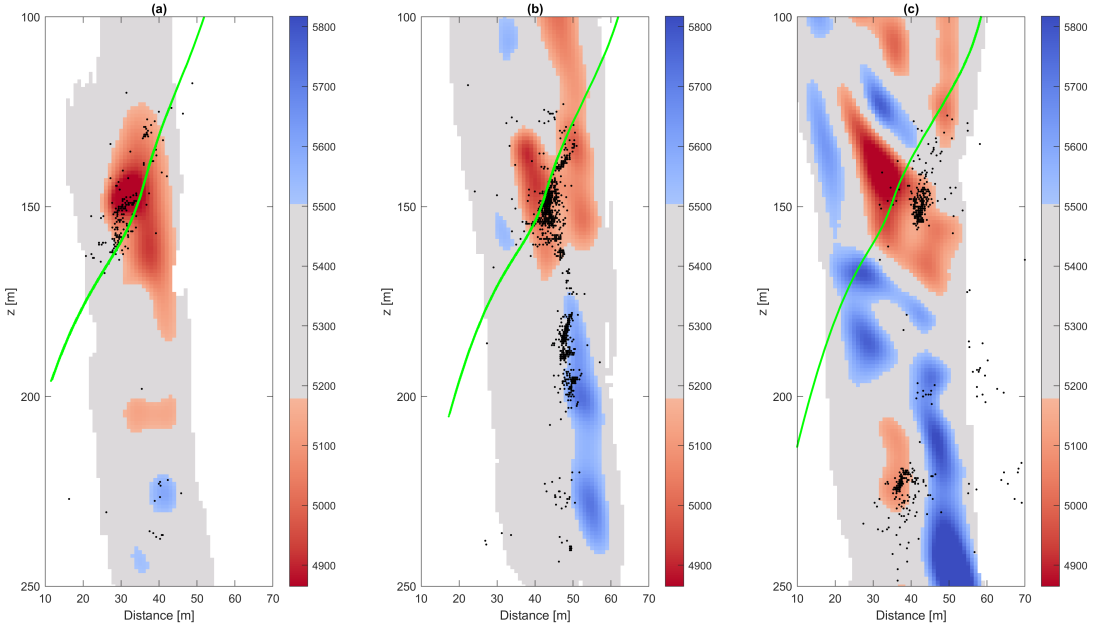

Figure 13. Vertical slices perpendical to the MFZ through the tomographic model. The slices are located near the trace of the injection borehole ST1 (roughly ±10 m away from each other). Low and high velocities are shown in red and blue, and intermediate velocity areas are shown gray. The seismicity located ~~±2.5 *m*~~ ±2.5 m distance from the slices is superimposed by black dots. The intersection of the MFZ is shown in light green.

with thin rays), because the sensitivity kernels ~~are governed primarily by the (prescribed) dominant wavelength of the seismic data~~(i.e., the fat ray volumes) are unaffected by the discretization of the inversion model.

There are two main findings from the analysis of the 3D velocity model derived with our tomography study. First, we could characterize ~~one of the major fault zones~~a major fault zone. Its signature in the tomographic image is not a narrow and well confined zone of decreased velocities, as one would expect. Instead, it is distinguished by a relatively large volume of generally decreased velocities with considerable heterogeneities. Checkerboard resolution tests indicated that some of the features may be due to the limited spatial resolution of our experimental setup, particularly near the boundaries of the region covered by the fat rays.

Secondly, we found a spatial correlation between passive seismic events, generated by hydraulic stimulations, and the ~~tomographically derived velocity structures . The passive~~ velocity structures in our tomographic model. The induced seismic events occur predominantly between high and very low velocity zones. Based on similar results from a small-scale laboratory study, we attribute this observation to the existence of stress gradients in the regions of intermediate velocities.

Data availability. The input data for the inversion is published by Maurer and Schwarz (2025): https://doi.org/10.3929/ethz-b-000725491. Seismicity catalogs of the VALTER project have been published by Rosskopf et al. (2024a)

Video supplement. Video supplements for the 3D velocity model are published by Maurer and Schwarz (2025) https://doi.org/10.3929/ethz-b-000725491

Appendix A: Appendix A: Checkerboard Tests

The spatial resolution of the tomographic inversions is a key information for interpreting the 3D tomograms. There are several options that can be considered for appraising the spatial resolution. For seismic tomography, so-called checkerboard tests established themselves to be a useful tool e(e.g., Zelt and Barton, 1998). Although such tests have well-known limitations (e.g., Leveque et al., 1993; Rawlinson and Spakman, 2016), they can provide a first-order estimate of the spatial resolution.

For checking the resolution power of our data set set, we generated synthetic data with block sizes of $5 \times 5 \times 5m^3$, $10 \times 10 \times 10m^3$ and $15 \times 15 \times 15m^3$. The same source-receiver configurations, as employed for the inversion of the observed data sets, were considered, and the same processing workflows were applied. The results are shown in Figures A1 to A3. They show selected slices through the 3D models. It is evident that block sizes of 15 and 10 metres can be generally well resolved, but structures of the size of 5 meters remain unresolved in most areas. It is also observed that the spatial resolution decreases, as expected, towards the boundaries of the regions covered by rays. This is particularly apparent in the horizontal slices in Figure A3.

Author contributions. MLS performed the data analysis, the Inversion and wrote the paper. HM supervised MLS, performed the earthquake relocation and wrote/edited the paper. AO and AS organized the data acquisition, performed preliminary tests and edited the paper. PAS edited the paper. HM, SW and DG supervised the project.

Competing interests. The authors declare that they have no conflict of interest.

Acknowledgements. In the "Bedretto Underground Laboratory for Geosciences and Geoenergies", ETH Zurich studies in close collaboration with national and international partners techniques and procedures for a safe, efficient, and sustainable use of geothermal heat and questions

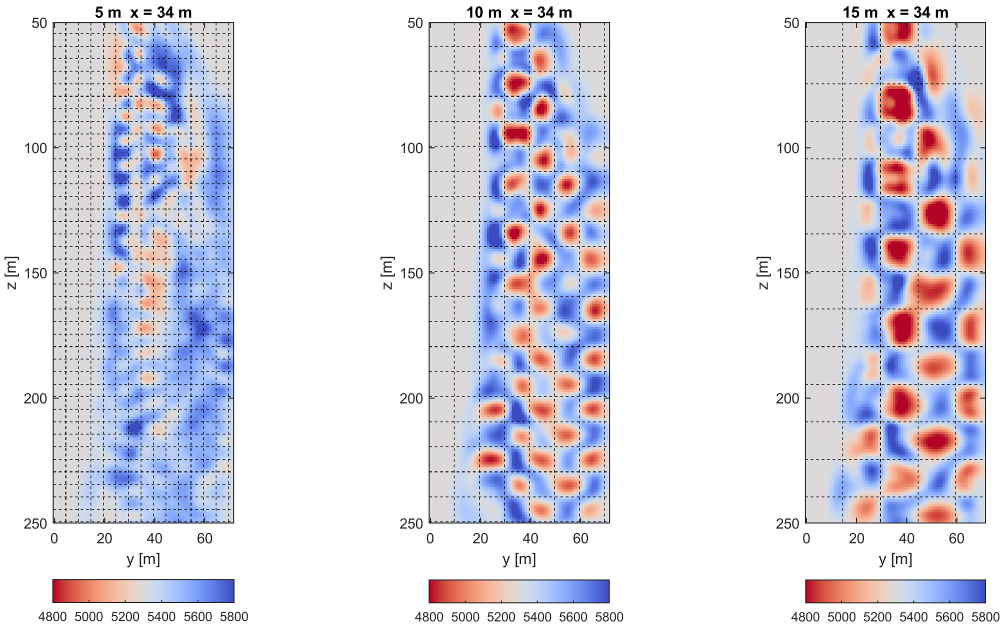

Figure A1. Vertical cross section along a y-z slize at x = 34 m. The dashed lines lines indicate the locations and size of the checkerboard blocks. Block sizes are 5 (left), 10 (middle) and 15 (right) metres.

related to earthquake physics. The BedrettoLab is financed by the Werner Siemens Foundation, ETH Zürich and the Swiss National Science Foundation. Miriam Schwarz is founded by the SNF Multi PhD (200021_192151) project. The research in this publication has received additional funding by the project VALTER (Validierung von Technologien zur Reservoir Entwicklung) (SI/501496-01). The BedrettoLab would like to thank Matterhorn Gotthard Bahn for providing access to the tunnel. We would like to thank Kai Bröker for his feedback on section 2, particularly regarding fracture mapping in the BedrettoLab. We thank the BedrettoLab Operation Team, led by Marian Hertrich, for their excellent support, which was essential for this project. This paper is BULGG publication BPN_029

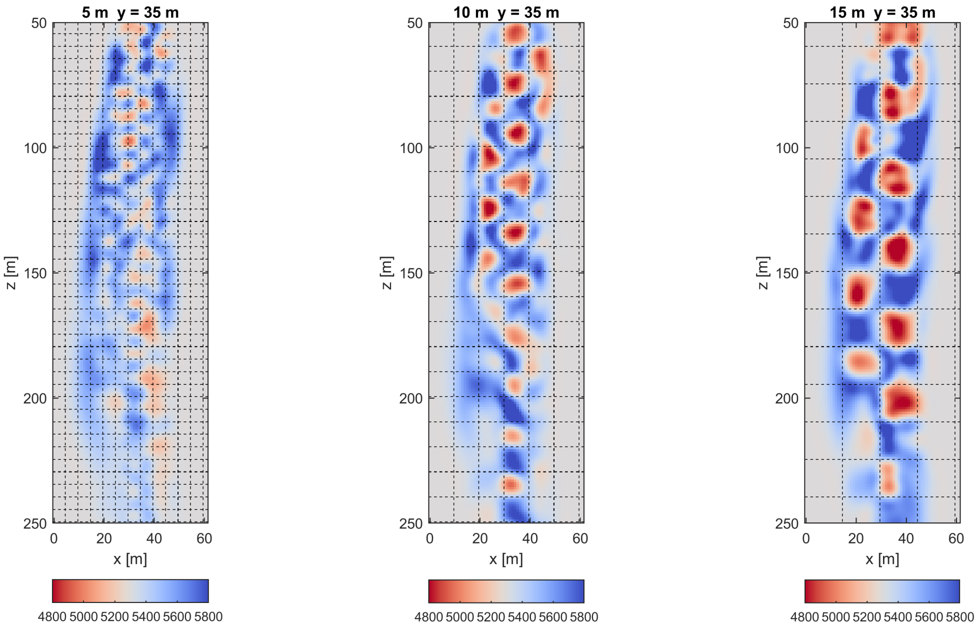

Figure A2. Vertical cross section along a x-z slize at y = 35 m. The dashed lines lines indicate the locations and size of the checkerboard blocks. Block sizes are 5 (left), 10 (middle) and 15 (right) metres.

References

Amann, F., Gischig, V., Evans, K., Doetsch, J., Jalali, R., Valley, B., Krietsch, H., Dutler, N., Villiger, L., Brixel, B., Klepikova, M., Kittilä, A., Madonna, C., Wiemer, S., Saar, M. O., Loew, S., Driesner, T., Maurer, H., and Giardini, D.: The seismo-hydromechanical behavior during deep geothermal reservoir stimulations: Open questions tackled in a decameter-scale in situ stimulation experiment, https://doi.org/10.5194/se-9-115-2018, 2018.

Barton, N.: Rock Quality, Seismic Velocity, Attenuation and Anisotropy, CRC Press, ISBN 9781134160136, https://doi.org/10.1201/9780203964453, 2006.

Behnen, K., Hertrich, M., Maurer, H., Shakas, A., Bröker, K., Epiney, C., Blanch Jover, M., and Giardini, D.: Investigation of Seismic Anisotropy in the Undisturbed Rotondo Granite, https://doi.org/10.5194/egusphere-2024-1919, 2024.

Block, L. V., Cheng, C. H., Fehler, M. C., and Phillips, W. S.: Seismic imaging using microearthquakes induced by hydraulic fracturing, Geophysics, 59, 102–112, https://doi.org/10.1190/geo1992-0156, 1994.

Bröker, K. and Ma, X.: Estimating the Least Principal Stress in a Granitic Rock Mass: Systematic Mini-Frac Tests and Elaborated Pressure Transient Analysis, Rock Mechanics and Rock Engineering, 55, 1931–1954, https://doi.org/10.1007/s00603-021-02743-1, 2022.

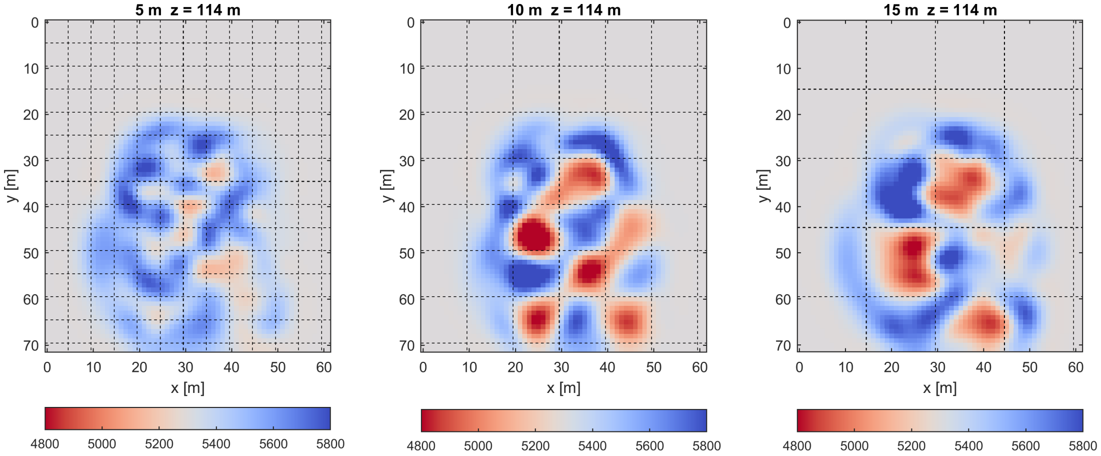

Figure A3. Horizontal cross section along a slice at z = 114 m. The dashed lines lines indicate the locations and size of the checkerboard blocks. Block sizes are 5 (left), 10 (middle) and 15 (right) metres.

Bröker, K., Ma, X., Gholizadeh Doonechaly, N., Rosskopf, M., Obermann, A., Rinaldi, A. P., Hertrich, M., Serbeto, F., Maurer, H., Wiemer, S., and Giardini, D.: Hydromechanical characterization of a fractured crystalline rock volume during multi-stage hydraulic stimulations at the BedrettoLab, Geothermics, 124, https://doi.org/10.1016/j.geothermics.2024.103126, 2024a.

Bröker, K., Ma, X., Zhang, S., Doonechaly, N. G., Hertrich, M., Klee, G., Greenwood, A., Caspari, E., and Giardini, D.: Constraining the stress field and its variability at the BedrettoLab: Elaborated hydraulic fracture trace analysis, International Journal of Rock Mechanics and Mining Sciences, 178, 105 739, https://doi.org/https://doi.org/10.1016/j.ijrmms.2024.105739, 2024b.

Ceccato, A., Behr, W. M., Zappone, A. S., Tavazzani, L., and Giuliani, A.: Structural Evolution, Exhumation Rates, and Rheology of the European Crust During Alpine Collision: Constraints From the Rotondo Granite—Gotthard Nappe, Tectonics, 43, https://doi.org/10.1029/2023TC008219, 2024.

Červený, V. and Soares, J. E. P.: Fresnel volume ray tracing, GEOPHYSICS, 57, 902–915, https://doi.org/10.1190/1.1443303, 1992.

Charléty, J., Cuenot, N., Dorbath, C., and Dorbath, L.: Tomographic study of the seismic velocity at the Soultz-sous-Forêts EGS/HDR site, Geothermics, 35, 532–543, https://doi.org/10.1016/j.geothermics.2006.10.002, 2006.

David, C., Nejati, M., and Geremia, D.: On petrophysical and geomechanical properties of Bedretto Granite, Tech. rep., https://doi.org..., 2020.

Deere, D. and Deere, D.: The Rock Quality Designation (RQD) in Practice, Rock Classification Systems for Engineering Purposes, ASTM STP 984, pp. 91–101, 1988.

Deere, D. and Miller, R.: Classification and index properties of intact roc, New Mexico, 1966.

Diehl, T., Cauzzi, C., Clinton, J., Kraft, T., Kästli, P., Massin, F., Lanza, F., Simon, V., Grigoli, F., Hobiger, M., Roth, P., Haslinger, F., Fäh, D., and Wiemer, S.: Earthquakes in Switzerland and surrounding regions during 2019 and 2020, Swiss Journal of Geosciences, 118, https://doi.org/10.1186/s00015-025-00489-4, 2025.

Doonechaly, N. G., Bröker, K., Hertrich, M., Rosskopf, M., Obermann, A., Durand, V., Serbeto, F., Shakas, A., Ma, X., Rinaldi, A. P., Repollés, V. C., Villiger, L., Meier, M.-A., Gischig, V., Plenkers, K., Maurer, H., Wiemer, S., and Giardini, D.: Insights from Subsurface Monitoring for Engineering of the Stimulation Pattern in Fractured Reservoirs, https://doi.org/10.21203/rs.3.rs-4859925/v1, 2024.

Edwards, B., Kraft, T., Cauzzi, C., Kästli, P., and Wiemer, S.: Seismic monitoring and analysis of deep geothermal projects in st Gallen and Basel, Switzerland, Geophysical Journal International, 201, 1022–1039, https://doi.org/10.1093/gji/ggv059, 2015.

Ellsworth, W. L., Giardini, D., Townend, J., Ge, S., and Shimamoto, T.: Triggering of the Pohang, Korea, Earthquake (Mw 5.5) by enhanced geothermal system stimulation, https://doi.org/10.1785/0220190102, 2019.

Escallon, D., Shakas, A., and Maurer, H.: Modelling and inferring fracture curvature from borehole GPR data: A case study from the Bedretto Laboratory, Switzerland, Near Surface Geophysics, 22, 235–254, https://doi.org/10.1002/nsg.12286, 2024.

Faulkner, D. R., Jackson, C. A., Lunn, R. J., Schlische, R. W., Shipton, Z. K., Wibberley, C. A., and Withjack, M. O.: A review of recent developments concerning the structure, mechanics and fluid flow properties of fault zones, https://doi.org/10.1016/j.jsg.2010.06.009, 2010.

Gischig, V. S., Giardini, D., Amann, F., Hertrich, M., Krietsch, H., Loew, S., Maurer, H., Villiger, L., Wiemer, S., Bethmann, F., Brixel, B., Doetsch, J., Doonechaly, N. G., Driesner, T., Dutler, N., Evans, K. F., Jalali, M., Jordan, D., Kittilä, A., Ma, X., Meier, P., Nejati, M., Obermann, A., Plenkers, K., Saar, M. O., Shakas, A., and Valley, B.: Hydraulic stimulation and fluid circulation experiments in underground laboratories: Stepping up the scale towards engineered geothermal systems, Geomechanics for Energy and the Environment, 24, https://doi.org/10.1016/j.gete.2019.100175, 2020.

Heidbach, O., Rajabi, M., Cui, X., Fuchs, K., Müller, B., Reinecker, J., Reiter, K., Tingay, M., Wenzel, F., Xie, F., Ziegler, M. O., Zoback, M. L., and Zoback, M.: The World Stress Map database release 2016: Crustal stress pattern across scales, https://doi.org/10.1016/j.tecto.2018.07.007, 2018.

Heincke, B., Maurer, H., Green, A. G., Willenberg, H., Spillmann, T., and Burlini, L.: Characterizing an unstable mountain slope using shallow 2D and 3D seismic tomography, Geophysics, 71, https://doi.org/10.1190/1.2338823, 2006.

Hirschberg, S., Wiemer, S., and Burgherr, P. e.: Energy from the earth Deep geothermal as a resource for the future?, TA-SWISS, 2015, https://doi.org/10.3929/ethz-a-010277690, 2015.

Holliger, K., Musil, M., and Maurer, H. R.: Ray-based amplitude tomography for crosshole georadar data: a numerical assessment, Tech. rep., www.elsevier.comrlocaterjappgeo, 2001.

Husen, S. and Kissling, E.: Local earthquake tomography between rays and waves: fat ray tomography, Tech. rep., ISBN 00319201/01, 2001.

Jordan, D.: Geological Characterization of the Bedretto Underground Laboratory for Geoenergies, ETH Zurich Research Collection, https://doi.org/10.3929/ethz-b-000379305, 2019.

Jordi, C., Schmelzbach, C., and Greenhalgh, S.: Frequency-dependent traveltime tomography using fat rays: application to near-surface seismic imaging, Journal of Applied Geophysics, 131, 202–213, https://doi.org/10.1016/j.jappgeo.2016.06.002, 2016.

Kijko, A.: An Algorithm for the Optimum Distribution of a Regional Seismic Network-I, Pageoph, 115, 999–1009, 1977.

Kneafsey, T., Dobson, P., Blankenship, D., Schwering, P., White, M., Morris, J. P., Huang, L., Johnson, T., Burghardt, J., Mattson, E., Neupane, G., Strickland, C., Knox, H., Vermuel, V., Ajo-Franklin, J., Fu, P., Roggenthen, W., Doe, T., Schoenball, M., Hopp, C., Tribaldos, V. R., Ingraham, M., Guglielmi, Y., Ulrich, C., Wood, T., Frash, L., Pyatina, T., Vandine, G., Smith, M., Horne, R., McClure, M., Singh, A., Weers, J., and Robertson, M.: The EGS Collab project: Outcomes and lessons learned from hydraulic fracture stimulations in crystalline rock at 1.25 and 1.5 km depth, Geothermics, 126, https://doi.org/10.1016/j.geothermics.2024.103178, 2025.

Labhart T: Erläuterungen Zum Geologischen Atlas Des Schweiz 1:25000, Val Bedretto, 2005.

Lanz, E., Maurer, H., and Green, A. G.: Refraction tomography over a buried waste disposal site, Geophysics, 63, 1414–1433, https://doi.org/10.1190/1.1444443, 1998.

Leveque, J.-J., Rivera, L., and Wittlinger, G.: On the use of the checker-board test to assess the resolution of tomographic inversions, https://academic.oup.com/gji/article/115/1/313/604170, 1993.

Li, B., Ding, L., Hu, D., and Zheng, S.: Backtracking Algorithm-based Disassembly Sequence Planning, in: Procedia CIRP, vol. 69, pp. 932–937, Elsevier B.V., ISSN 22128271, https://doi.org/10.1016/j.procir.2017.12.007, 2018.

Lützenkirchen, V. and Loew, S.: Late Alpine brittle faulting in the Rotondo granite (Switzerland): Deformation mechanisms and fault evolution, Swiss Journal of Geosciences, 104, 31–54, https://doi.org/10.1007/s00015-010-0050-0, 2011.

Ma, X., Hertrich, M., Amann, F., Bröker, K., Doonechaly, N. G., Gischig, V., Hochreutener, R., Kästli, P., Krietsch, H., Marti, M., Nägeli, B., Nejati, M., Obermann, A., Plenkers, K., Rinaldi, A. P., Shakas, A., Villiger, L., Wenning, Q., Zappone, A., Bethmann, F., Castilla, R., Seberto, F., Meier, P., Driesner, T., Loew, S., Maurer, H., Saar, M. O., Wiemer, S., and Giardini, D.: Multi-disciplinary characterizations of the BedrettoLab-A new underground geoscience research facility, Solid Earth, 13, 301–322, https://doi.org/10.5194/se-13-301-2022, 2022.

Maurer, H. and Green, A. G.: Potential coordinate mislocations in crosshole tomography: Results from the Grimsel test site, Switzerland, Tech. Rep. 6, http://pubs.geoscienceworld.org/geophysics/article-pdf/62/6/1696/3172949/1696.pdf, 1997.

Maurer, H. and Schwarz, M. L.: Data collection to: New insights on the fault structure of a geothermal testbed and the associated seismicity based on active seismic tomography, https://doi.org/10.3929/ETHZ-B-000725491, 2025.

Maurer, H., Holliger, K., and Boerner, D. E.: Stochastic regularization: Smoothness or similarity?, Geophysical Research Letters, 25, 2889–2892, https://doi.org/10.1029/98GL02183, 1998.

Mavko, G., Mukerji, T., and Dvorkin, J.: The Rock Physics Handbook, Cambridge University Press, 2nd edition edn., ISBN 9780521861366, https://doi.org/10.1017/CBO9780511626753, 2009.

Meier, M.: Geological characterisation of an underground research facility in the Bedretto tunnel, ETH Zurich Research Collection, https://doi.org/10.3929/ethz-b-000334001, 2017.

Menke, W.: Geophysical Data Analysis: Discrete Inverse Theory, Elsevier, ISBN 9780124909205, https://doi.org/10.1016/B978-0-12-490920-5.X5001-7, 1984.

Moser, T. J., Van Eck, T., and Nolet, G.: Hypocenter determination in strongly heterogeneous Earth models using the shortest path method, Journal of Geophysical Research, 97, 6563–6572, https://doi.org/10.1029/91JB03176, 1992.

Nakagome, O., Uchida, T., and Horikoshi, T.: Seismic reflection and VSP in the kakkonda geothermal field, japan: fractured reservoir characterization, Geothermics, 27, 535–552, https://doi.org/10.1016/S0375-6505(98)00032-7, 1998.

Nakata, N., Vasco, D. W., Shi, P., Bai, T., Lanza, F., Dyer, B., Chen, C., Park, S.-E., and Qiu, H.: Elastic Characterization at Utah FORGE: P-wave Tomography and VSP Subsurface Imaging, Tech. rep., 2023.

Nolet, G.: Seismic Tomography, Springer Netherlands, Dordrecht, ISBN 978-90-277-2583-7, https://doi.org/10.1007/978-94-009-3899-1, 1987.

Obermann, A. and Hillers, G.: Seismic time-lapse interferometry across scales, in: Advances in Geophysics, vol. 60, pp. 65–143, Academic Press Inc., ISBN 9780128175484, https://doi.org/10.1016/bs.agph.2019.06.001, 2019.

Obermann, A., Wu, S. M., Ágústsdóttir, T., Duran, A., Diehl, T., Sánchez-Pastor, P., Kristjansdóttir, S., Hjörleifsdóttir, V., Wiemer, S., and Hersir, G. P.: Seismicity and 3-D body-wave velocity models across the Hengill geothermal area, SW Iceland, Frontiers in Earth Science, 10, https://doi.org/10.3389/feart.2022.969836, 2022.

Obermann, A., Rosskopf, M., Plenkers, K., Broeker, K., Rinaldi, A., Doonechaly, N., Gischig, V., Zappone, A., Amann, F., Cocco, M., Hertrich, M., Jalali, M., Junker, J., Kästli, P., Ma, X., Maurer, H., Meier, M.-A., Schwarz, M., Selvadurai, P., and Giardini, D.: Seismic response of hectometer-scale fracture systems to hydraulic stimulation in the Bedretto Underground laboratory, Switzerland, Journal of Geophysical Research: Solid Earth, https://doi.org/10.1029/2024JB029836, 2024.

Olasolo, P., Juárez, M. C., Morales, M. P., Damico, S., and Liarte, I. A.: Enhanced geothermal systems (EGS): A review, https://doi.org/10.1016/j.rser.2015.11.031, 2016.

Paige, C. C. and Saunders, M. A.: LSQR: An Algorithm for Sparse Linear Equations and Sparse Least Squares, pp. 43–71, 1982.

Paterson, M. S. and Wong, T.-f.: Experimental Rock Deformation – The Brittle Field, Springer-Verlag Berlin Heidelberg 2005, second edition edn., ISBN 978-3-540-24023-5, 2005.

Place, J., Sausse, J., Marthelot, J. M., Diraison, M., Géraud, Y., and Naville, C.: 3-D mapping of permeable structures affecting a deep granite basement using isotropic 3C VSP data, Geophysical Journal International, 186, 245–263, https://doi.org/10.1111/j.1365-246X.2011.05012.x, 2011.

Plenkers, K., Manthei, G., and Kwiatek, G.: Underground In-situ Acoustic Emission in Study of Rock Stability and Earthquake Physics, in: Springer Tracts in Civil Engineering, pp. 403–476, Springer Science and Business Media Deutschland GmbH, https://doi.org/10.1007/978-3-030-67936-1_16, 2022.

Podvin, P. and Lecomte, I.: Finite difference computation of traveltimes in very contrasted velocity models: a massively parallel approach and its associated tools, Tech. rep., https://academic.oup.com/gji/article/105/1/271/671376, 1991.

Pratt, R. G. and Worthington, M. H.: The application of diffraction tomography to cross-hole seismic data, Geophysics, 53, 1284–1294, https://doi.org/10.1190/1.1442406, 1988.

Rast, M., Galli, A., Ruh, J. B., Guillong, M., and Madonna, C.: Geology along the Bedretto tunnel: kinematic and geochronological constraints on the evolution of the Gotthard Massif (Central Alps), Swiss Journal of Geosciences, 115, https://doi.org/10.1186/s00015-022-00409-w, 2022.

Rawlinson, N. and Spakman, W.: On the use of sensitivity tests in seismic tomography, Geophysical Journal International, 205, 1221–1243, https://doi.org/10.1093/gji/ggw084, 2016.

Rosskopf, M., Durand, V., Plenkers, K., Villiger, L., Giardini, D., and Obermann, A.: Accuracy of picoseismic catalogs in hectometer-scale in-situ experiments, https://doi.org/10.22541/essoar.172736342.25689581/v1, 2024a.

Rosskopf, M., Durand, V., Villiger, L., and Doetsch, J.: DUGseis: A Python package for real-time and post-processing of picoseismicity, https://doi.org/10.21105/joss.06768ï, 2024b.

Salazar Vásquez, A. F., Selvadurai, P. A., Bianchi, P., Madonna, C., Germanovich, L. N., Puzrin, A. M., Wiemer, S., Giardini, D., and Rabaiotti, C.: Aseismic strain localization prior to failure and associated seismicity in crystalline rock, Scientific Reports, 14, https://doi.org/10.1038/s41598-024-75942-9, 2024.

Sergeev, S. A., Meier, M., and Steiger, R. H.: EPSL Improving the resolution of single-grain U/Pb dating by use of zircon extracted from feldspar: Application to the Variscan magmatic cycle in the central Alps, Tech. rep., 1995.

Shakas, A.: Borehole Logging Data from Characterization Boreholes in Bedretto Underground Lab for Geoenergies, 2019.

Stanchits, S., Mayr, S., Shapiro, S., and Dresen, G.: Fracturing of porous rock induced by fluid injection, Tectonophysics, 503, 129–145, https://doi.org/10.1016/j.tecto.2010.09.022, 2011.

Townend, J. and Zoback, M. D.: How faulting keeps the crust strong, GEOLOGY, 28, 399–402, 2000.

Williamson, P. R. and Worthington, M. H.: Resolution limits in ray tomography due to wave behavior: numerical experiments, Geophysics, 58, 727–735, https://doi.org/10.1190/1.1443457, 1993.

Woodward, M. J.: Wave-equation tomography, Geophysics, 57, 15–26, https://doi.org/10.1190/1.1443179, 1992.

Zang, A., Niemz, P., Specht, S. V., Zimmermann, G., Milkereit, C., Plenkers, K., and Klee, G.: Comprehensive data set of in situ hydraulic stimulation experiments for geothermal purposes at the Äspö Hard Rock Laboratory (Sweden), Earth System Science Data, 16, 295–310, https://doi.org/10.5194/essd-16-295-2024, 2024.

Zelt, C. A. and Barton, P. J.: Three-dimensional seismic refraction tomography: A comparison of two methods applied to data from the Faeroe Basin, https://doi.org/10.1029/97jb03536, 1998.